Four-dimensional *in vivo* dosimetry by dose reconstruction using continuous EPID images and phase sorting method

by

JiHyung Yoon

July, 2015

Director of Dissertation: Dr. Jae Won Jung

Major Department: Physics

In vivo dosimetry is widely used for patient specific dose evaluation and treatment verification in external beam radiation therapy (EBRT). There is a growing interest in using an electronic portal imaging device (EPID) for *in vivo* dosimetry, by correlating pixel values of measured EPID images to three-dimensional (3D) dose in the patient. In this research, a non-iterative dose reconstruction method has been employed, which utilizes phantom and EPID response functions calculated from pre-acquired Computed Tomography (CT) image and simulated EPID image from Monte Carlo (MC) simulation. The accuracy of reconstructed dose, however, is limited by that of the simulated EPID image. In this study, a previously proposed density scaled model in XVMC code has been improved by physically relevant effective atomic number modeling and employing realistic phase space data. The new model has been tested under various field sizes and phantom thickness, including homogeneous and heterogeneous media. It has been shown that the calculated EPID images from the new EPID model are agreeable to the measured EPID images after field size and phantom thickness factors applied.

The improved EPID model in MC code has been used in four-dimensional (4D) dose reconstruction. Considering the patient respiratory motion, breathing phase of acquired EPID

images are determined by the phase sorting method for various treatment plans. For each phase, dose reconstruction has been performed using the sorted EPID images and 4D CT image of corresponding phase. The reconstructed 3D doses of each phase have been transformed to a reference phase to calculate the accumulated dose. The reconstructed doses have been shown good agreements to the forward 4D calculation in gamma analysis and dose-volume histogram (DVH) comparison. Based on the results, the new EPID model and the suggested phase sorting method accurately reconstruct the dose to the phantom for the cases shown in this study.

Four-dimensional *in vivo* dosimetry by dose reconstruction using continuous EPID images and phase sorting method

A Dissertation

Presented to the Faculty of the Department of Physics

East Carolina University

In Partial Fulfillment of the Requirements for the Degree

Doctoral of Philosophy in Biomedical Physics

by

JiHyung Yoon

July, 2015

Four-dimensional *in vivo* dosimetry by dose reconstruction using continuous EPID images and phase sorting method

by

JiHyung Yoon

APPROVED BY:

DIRECTOR OF
DISSERTATION:_____
Jae Won Jung, Ph.D.

COMMITTEE MEMBER: _____
Michael Dingfelder, Ph.D.

COMMITTEE MEMBER: _____
Yuanming Feng, Ph.D.

COMMITTEE MEMBER: _____
Zhibin Huang, Ph.D.

COMMITTEE MEMBER: _____
Jefferson Shinpaugh, Ph.D.

CHAIR OF THE DEPARTMENT
OF PHYSICS:_____
Jefferson Shinpaugh, Ph.D.

DEAN OF THE
GRADUATE SCHOOL: _____
Paul J. Gemperline, PhD

ACKNOWLEDGEMENTS

I would like to express my appreciation to my advisor, Dr. Jae Won Jung, for unlimited support in academic research and also as a mentor. He encouraged me to think and provided invaluable suggestions. I also thank to my committee members, Dr. Michael Dingfelder, Dr. Yuanming Feng, Dr. Zhibin Huang and Dr. Jefferson Shinpaugh for their valuable time and feedback.

I also thank to Dr. Inwhan Yeo, for the all the moments of discussion about the experiment and data analysis. Also, I thank to Dr. Jong Oh Kim for support of Monte Carlo simulations and code development. I would also like to thank Dr. B. Yi, for supporting ideas and feedbacks of the experimental method and the digital phantom.

In addition, I am also thankful for my colleague Chris Pelletier for all his helps, comments, and ideas. Finally, I thank to my wife, Kyusun Hwang, for her great support and taking care of me all the time.

TABLE OF CONTENTS

LIST OF TABLES

LIST OF FIGURES

LIST OF ABBREVIATIONS

AIP	Average Intensity Projection
CBCT	Cone Beam Computed Temography
CCD	Charge-Coupled Device
CT	Computed Tomography
CTV	Clinical Target Volume
DD	Dose Difference
DRR	Digitally Reconstructed Radiograph
DTA	Distance to Agreement
DVH	Dose Volume Histogram
EBRT	External Beam Radiation Therapy
EGS	Electron Gamma Shower
EPID	Electronic Portal Imaging Device
FPS	Frames per Second
IC	Ion Chamber
IMRT	Intensity Modulated Radiation Therapy
LINAC	Linear Accelerator
MC	Monte Carlo
MIP	Maximum Intensity Projection
MLC	Multi Leaf Collimator
MOSFET	Metal-Oxide-Semiconductor Field-Effect-Transistor
PTV	Planning Target Volume
QA	Quality Assurance
TAR	Tissue Air Ratio

TLD	Thermoluminescent Dosimeter
TPS	Treatment Planning System
VMAT	Volumetric Modulated Arc Therapy
XCAT	Extended Cardio-Torso
XVMC	X-ray Voxel Monte Carlo

1. INTRODUCTION

External radiation therapy is widely being used for the purpose of cancer treatment. To minimize dose to healthy organs while maximizing treatment efficiency, intensity modulated radiation therapy (IMRT) technique is finding increased used. It utilizes intensity modulated irradiation, either by attenuation through Cerrobend block or through multi-leaf collimators (MLCs), to define field shape. For the latter method, the accumulated 3-dimensional dose distribution can be achieved by step-and-shoot or dynamic MLCs, which combine multiple field shapes defined by collimators. However, in the added complexity of IMRT compared to simple open field requires more sophisticated treatment planning and dose estimation. Since the dose calculation in the for IMRT treatment planning required complex calculation, using a treatment planning system, instead of hand calculation, was suggested [1]. The generated plan was evaluated by performing a quality assurance (QA) test, where it was suggested that the pretreatment QA method should be optimized to evaluate complex IMRT treatment plan [2]. In many cases, however, it was reported that IMRT treatment was not always accurately delivered as planned [3]. Therefore, there had been increasing interest for the evaluation of actual received dose during treatment [4]–[9].

An electronic portal imaging device (EPID) is proposed as a convenient tool for *in vivo* dosimetry that does not require additional setup process, and therefore reduces time and burden for *in vivo* dosimetry in many clinical institutes. Some researchers suggested EPID dosimetry as an essential component of IMRT QA [10]. Also, EPID based real-time treatment verification method was studied [11].

In this study, a method for the calculation of actual received dose to the patient from external beam radiation therapy (EBRT) was proposed. A dose reconstruction method based on acquired cine EPID images, which are acquired in continuous time frame during the treatment and patient 4D CT images was used for this purpose. For this, the previously developed EPID image prediction model was improved in Monte Carlo (MC) simulation. The calculated EPID images from the improved model were used to determine patient's breathing phase of acquired EPID images. The use of EPID as an *in vivo* dosimeter will enable not only real-time treatment evaluation, but also adaptation treatment planning.

1.1*In vivo* dosimetry

To deliver dose to a patient accurately as desired, pretreatment verification is necessary. In pretreatment verification, the dose in an idealized condition (for example, homogeneous flat water phantom at the isocenter) calculated from a treatment planning system (TPS) is compared with the measured dose. The difference between measurement and planning is quantified by the gamma index [12] to express level of agreement, which usually allows 3% of dose difference (DD) or 3 mm distance to agreement (DTA) at a point in many institutions. Later, a more accurate geometrical interpolation method, which interpolates values between two points in 3-dimensional vector space, for gamma index calculation was suggested [13]. The pretreatment verification ensures the machine parameters, such as gantry and MLC motion, dose rate, and couch motion are within acceptable parameters. However, IMRT pretreatment QA does not

predict patient dose error, since it does not contain any patient information in the measurement [14].

While pretreatment verification does not involve in patient, *in vivo* dosimetry requires dose evaluation to an actual patient. *In vivo* is Latin for "within the living", which denotes the use of a living organism for a specific purpose, as opposed to *ex vivo* or *in vitro*. In external radiation therapy, *in vivo* dosimetry implies the measurement of actual received dose to the patient from the radiation during the treatment. However, since measuring the dose in the patient body directly is clinically unavailable, the doses in the patient's body are correlated by known relations to the measured values from the dosimeter which is placed outside or near the point of interest. The patient specific QA is performed by *in vivo* dosimetry which is measuring dose in the patient's body with such an indirect method. Some researchers, however, did not regard the devices placed at the entrance side of the patient (e.g., monitoring chamber in the linac head) as *in vivo* dosimeters, since they did not provide patient specific information [7].

There are several commonly used *in vivo* dosimeters to measure dose from the external radiation. Thermoluminescent dosimeter (TLD) have been widely used to measure accumulated dose during a certain time period to workers under radiation environment, or to measure dose to a patient from EBRT or brachytherapy [15]. The TLD materials store absorbed radiation energy in metastable states and release energy in the form of visible light when heated. The dose to the TLD is measured by the amount of light released, which is proportional to the accumulated absorbed dose to the TLD; therefore, it is not suitable for time-resolved *in vivo* dosimetry. Time-resolved dosimeters include diode, metal-oxide semiconductor field effect transistors (MOSFET) and electronic portal imaging device (EPID). They are able to measure energy deposition in real-time and the measurement can be read during the treatment. However, diode and MOSFET

dosimeters need to be recalibrated after receiving a large dose, which limits continuous usage of the dosimeter. The EPID is initially developed for acquisition of MV portal image replacing the use of film. Since the EPID does not require additional setup process and is able to obtain 2D images, it is a good candidate for *in vivo* dosimetry in EBRT [7], [16].

Using the EPID is an ideal solution for *in vivo* dosimetry that allows to reduce time and effort when compare to other available methods, and therefore can be implemented easily [16]. To use the EPID as an *in vivo* dosimeter, however, the relationship between the EPID image and the dose to the patient should be determined based on a patient specific method. The dose reconstruction method, which correlates the EPID image and the patient dose, is described in the following section.

1.2Dose reconstruction

As treatment planning becomes increasingly complex, accurate evaluation of the dose to the patient becomes more important. Therefore, dose reconstruction methods have been studied by many researchers [11], [17]–[24]. There are two approaches to calculate dose to a patient; forward calculation and backward reconstruction. In the forward approach, the dose to the patient is calculated based on the information of incident beam to the patient [17], [18], [23]. Some researchers utilized Dynalog file to determine MLC position and field shape for dose calculation [17], [18]. However, it was reported that mismatches between Dynalog file and real MLC positions were observed in some studies [17], [24], [25]. Another group suggested to use measured EPID images to determine MLC positions [11], [19], [26]. They calculated the patient

dose with MLC positions obtained from the EPID image, but did not use pixel values, which containing attenuation information from the patient, on the image for the dose calculation. The second approach is backward dose reconstruction; the measured EPID images during the treatment were utilized for the dose calculation [27]–[30]. In this approach, dose to a point in the patient was correlated to a pixel value on the EPID image. Since transmitted radiation through the patient contains valuable information, the backward dose reconstruction method can be used for *in vivo* dosimetry [28], [31]–[33].

McNutt *et al.* proposed an iterative convolution/superposition algorithm [27] to reconstruct patient dose. Jarry *et al.* suggested a dose reconstruction method in 4 steps [34]; (1) MC dose calculation, (2) portal image processing, (3) MC phase space reconstruction and (4) MC dose and portal image reconstruction. Yeo *et al.* introduced a non-iterative patient-specific dose reconstruction method [35] which utilizes EPID images and the patient CT. They suggested generating a phantom response function from the incident beam by Monte Carlo calculation. To calculate dose from acquired EPID image, the relationship between predicted EPID image and the phantom dose was established (Figure 1).

Figure 1 shows a simplified method of the dose reconstruction model. The phantom dose can be calculated by the equation

$$\underline{P} = \underline{\underline{R_P}} \cdot \underline{\underline{R_E^{-1}}} \cdot \underline{E} \qquad (1)$$

where $\underline{\underline{R_P}}$ is a 2-dimensional phantom response function and $\underline{\underline{R_E}}$ is a 2-dimendional EPID response function, respectively. $\underline{\underline{R_P}}$ and $\underline{\underline{R_E}}$ are calculated from Monte Carlo simulation. $\underline{E}$ is the

measured EPID image and the phantom dose $\underline{P}$ is reconstructed by the equation. The phantom response function $\underline{\underline{R_P}}$ and EPID response function $\underline{\underline{R_E}}$ are patient specific functions; if patient anatomy is changed, $\underline{\underline{R_P}}$ and $\underline{\underline{R_E}}$ also have to be recalculated accordingly.

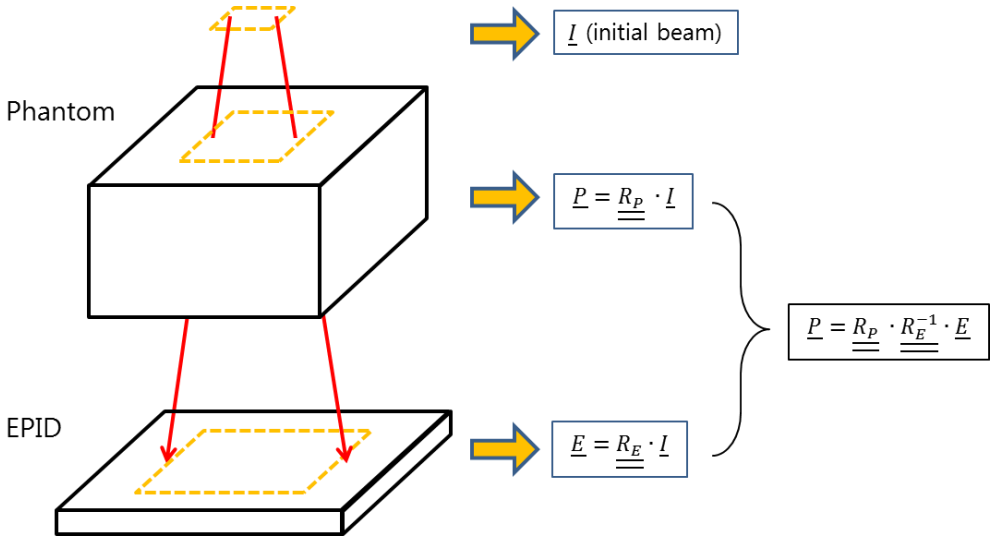

Figure 1. Phantom response functions in dose reconstruction model. (The picture was reproduced from Yeo et al., 2009 [35])

In this study, the non-iterative method suggested by Yeo *et al.* [35] was employed for the dose reconstruction. The accuracy of reconstructed dose from this method is limited by the accuracy of patient CT and EPID image prediction model in Monte Carlo simulation. However, improving the accuracy and quality of CT image is beyond the scope of this study. Instead, the

accuracy of the EPID image prediction model was improved in this study to provide better agreement between predicted and measured images by introducing the realistic physical structure of EPID in fast Monte Carlo code.

1.3Structure of EPID

The EPID was initially developed to replace conventional film portal imaging used in pretreatment patient alignment. Later, researchers found its usefulness as an *in vivo* dosimeter. Since the EPID is attached to the linac, it does not require additional setup process, unlike other *in vivo* dosimeters.

Among many types of EPID, amorphous silicon (aSi) is widely being used because of its ability to provide high resolution; linear dose and dose rate response; better image quality compared with the other types of EPID, such as ion chamber (IC) matrix or CCD camera; and higher sensitivity, less dose per image. The aSi EPID is composed of metal plate, phosphor layer, photodiode, capacitor, glass plate and electronic circuits. In phosphor layer, visible photons are generated by incident high energy X-rays. Then, the generated visible photons produce electron-hole pairs in the photodiode. Finally, the electron charges are stored in the capacitor. (Figure 2)

To construct a two-dimensional image, the electronic circuit periodically reads accumulated electrons captured in the capacitive storage. The read-out process is performed by a line after another, where a line is formed by one dimensional array of capacitors. Therefore, capacitive storages are “dumped” periodically by the circuit, enabling to measure high dose rate.

The read-out circuit transfer one-dimensional image information to the image processing unit and the 2D image is constructed [36].

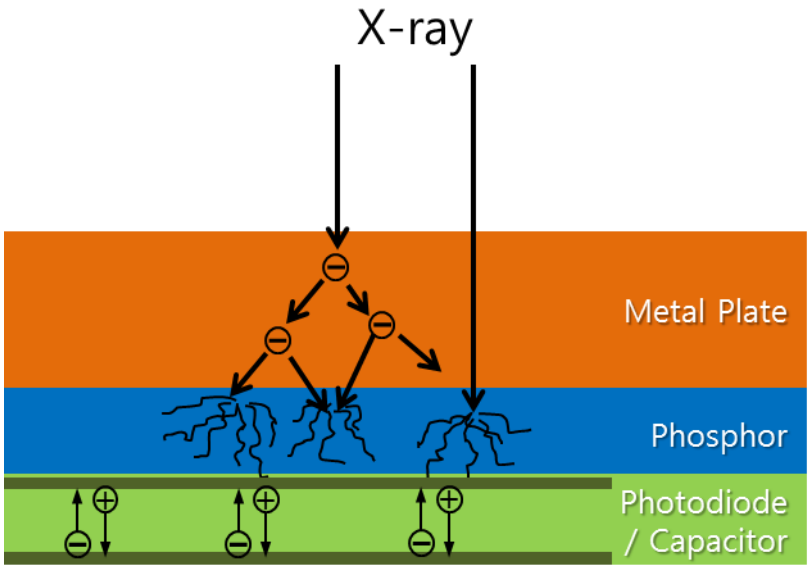

Figure 2. Schematic illustration (not in scale) of interactions in the structure of a pixel in EPID. (The picture was reproduced from Antonuk et al., 2002 [37])

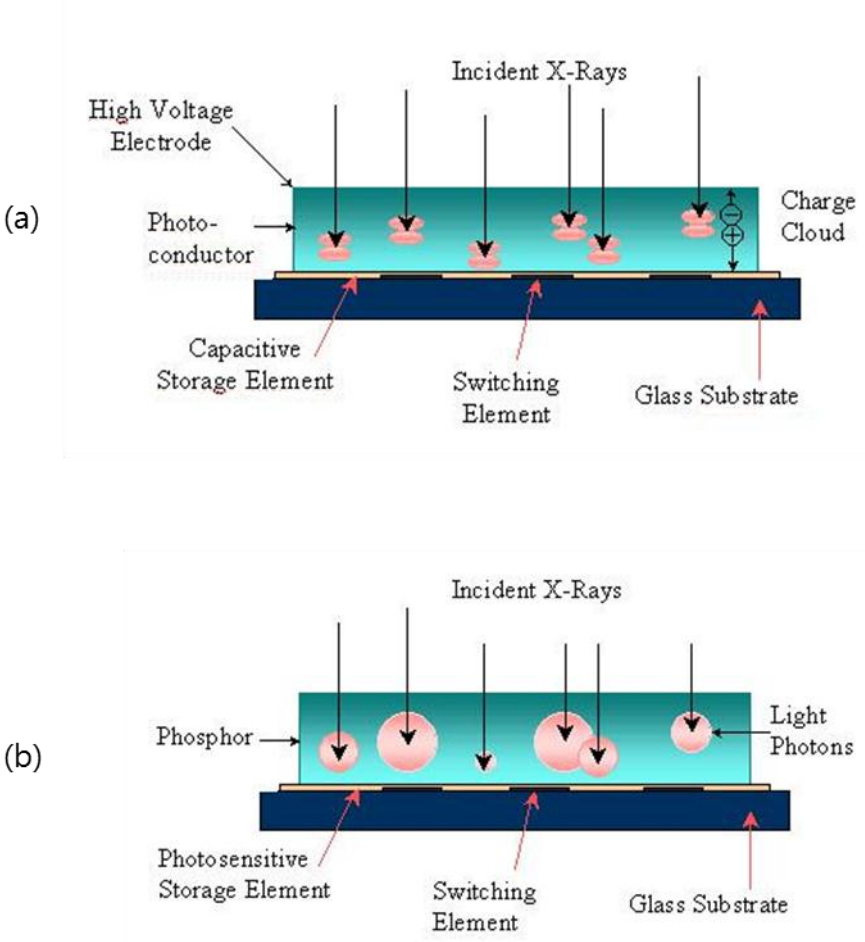

Figure 3. Schematic illustration of (a) direct detection method with the phosphor layer and (b) indirect detection method [38].

The response of EPID is known to be linearly proportional to total dose or dose rate. Therefore, some researchers suggested to use the EPID as a dosimeter [39]. However, it was found that the response of the EPID was not linear to the incident energy of photons. Some researchers studied characteristic of EPID without phosphor layer [37]. In this method, the incident photon directly interacts with the photodiode. There are two methods for the image detection of the aSi EPID, as shown in Figure 3. For direct detection method, the incident x-ray

interacts with the photo capacitor directly, by generating electron/hole pair in the photodiode. In this method, the response of the EPID is linearly proportional to the ion chamber. For indirect method, however, incident x-ray interacts with phosphor layer and visible light is generated. Then, the generated photon is detected in the photodiode. While indirect method has many advantages [37], such as fast response and low dose per image, its response is dependent on field size [40]. Also, it was reported that it has hypersensitivity to lower energy (<1 MeV) photons [41]. El-Mohri *et al.* [42] tested EPID characteristics with and without phosphor layer and concluded that indirect (with phosphor layer) method provides better sensitivity, where direct method (without phosphor layer) yields the similar linear responses to the ion chamber. Also, the response varies by upper phantom thickness and field size [43], which can be attributed to an increase in the low energy scattered component, leading to an over response in the EPID. Therefore, the EPID response, measured by pixel value in the subsequent image, is not linearly proportional to the dose in water phantom.

The read-out is not an instantaneous process; the image acquisition requires a short time period to read throughout two-dimensional photo capacitor array on the EPID. This time delay results in banding artifact on the acquired image, as shown in Figure 4. Woodruff *et al.* suggested taking average of 3 images to eliminate the patterning issue [44]. Therefore, useful image can be obtained by averaging subsequent images to reduce the patterning effect due to the synchronization with the frequency of linac accelerator and the EPID readout timing. The banding artifact can be reduced by choosing a lower frame rate that provides averaged images over several frames. Current EPID provides a maximum 10 frames per second (aS500) with averaged images by internal software [37], thus the banding artifact is not shown in the acquired

image. However, the acquired image still has delay or lag under some conditions, especially when field shape is changed during image acquisition [45].

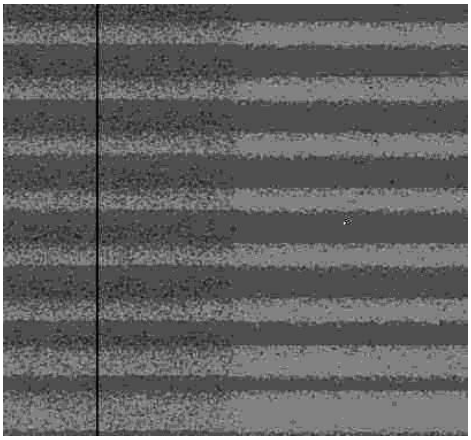

Figure 4. An example of banding artifact on EPID image. The image was acquired with flood field and the exposure time was 200 μs. The image level was adjusted by brightness +65% and contrast +80% to enhance the artifact. (Measured with Pelkin Elmer XRD 0822 Digital X-Ray Detector)

Despite these limitations, such as over-sensitivity to lower energy photons and banding artifact issue, EPID is still a good candidate for *in vivo* dosimetry. There have been many efforts to use the aSi EPID for absolute dosimetry for pre-treatment verification[46]. However, due to its non-linearity response to the ion chamber, the EPID cannot be modeled by simple homogeneous water medium and therefore how to predict an accurate EPID image is a key to success in *in vivo* dosimetry using the EPID.

1.4EPID modeling in Monte Carlo codes

Offering on-line exit dose, electronic portal imaging devices (EPID) have been employed for *in vivo* dosimetry of radiation deliveries [5]–[8]. For treatment verification using EPID, various computational models of the dose image of EPID have been developed [47]–[60]. Among them, the most utilized models are characterized by the use of kernels that are pre-determined dose responses of primary and scattered fluences in EPID [47]–[54]. The kernel-based models have been widely used due to their fast calculation speed and reasonable accuracy. The accuracy of the models was improved by employing kernels based on Monte Carlo simulations of EPID [55]–[57]. However, it was reported that the dose calculation from Monte Carlo simulation is more accurate than using advanced kernel methods in most cases [61]. Where it was not tested in the EPID plane, one may expect that a full Monte Carlo simulation for an EPID image prediction is more accurate, not requiring empirical or Monte Carlo based pre-calculated kernels.

A continuous effort was exerted to achieve the maximum possible accuracy by modeling details of actual structures of EPID and their elemental compositions in a Monte Carlo code. The model allowed direct radiation transport through the structures without utilizing the kernels. Among them, Siebers *et al.* modeled EPID (aS500 Varian Medical Systems, Inc.) with a virtual detector[58] technique utilizing detector grids in the dose calculation region only, instead of performing voxelized calculations across the entire radiation transport media in the EGS4/DOSXYZ user code [62] which requires a longer calculation time. The model was not tested where phantoms were placed above the EPID. The test, however, is necessary for its application in exit dose verification (i.e. exit dosimetry) at a distance from the isocenter. This is

because the exit dose calculation under the phantom located at isocenter is difficult than without intervening phantoms by involving radiation transport through heterogeneous media and air gaps. Such model, therefore, in principle could be vulnerable to changes in phantom and air gap thicknesses and the related scattering contributions [63], [64].

EGSnrc is known as the most accurate Monte Carlo code for external radiation dose calculation [65], [66] but requires longer calculation time, up to 48 times compared with other MC codes [67], [68]. Therefore, efforts to speed up calculation time of EGSnrc/DOSXYZnrc by modified calculation method [69] or using GPU [70] were heavily studied. While they showed improvement, it was not fast enough for clinical use. Meanwhile, a simplified and fast calculation model of EPID based on MC transport for exit dosimetry was introduced by Jung *et al.* [71] The model incorporates structural and elemental composition of EPID (aS1000) by homogenized (i.e., water) layers in the XVMC code [72]. To account for heterogeneity in the actual composition of EPID structures, each homogeneous layer was assigned the physical density of the corresponding structure. While the model produced acceptable accuracy in a relatively fast computation time, it generated EPID image responses that are highly dependent on the variation of attenuation thicknesses in patient, thus requiring thickness-dependent factors that account for differences between measured and calculated EPID images and showed limited agreement in the region of beam penumbra.

The XVMC code simulates voxelized volume to reduce calculation time. Also, to simplify calculation, it assumes materials in the simulation as water equivalent; the different media was determined by the difference in density. While EGSnrc, which is regarded as the gold standard in the external beam simulation, calculates all physical interactions with materials by

atomic number modeling, XVMC approximates the interaction with media [72], [73]. The Compton scattering is calculated by exactly the same mechanism as in EGS, while the dose from photoelectric effect is locally deposited in the voxel where the event occurred. This approximation yields fast and relatively accurate results in water-equivalent phantom; however, it cannot simulate atomic composition, and therefore the accuracy decreases for higher atomic number materials. Therefore, the effect from higher atomic number should be corrected.

In this study, for exit dosimetry applications, a new virtual detector model in the EGSnrc code [74] was developed and the EPID model in the XVMC code was improved by considering the effective atomic number of each EPID layer and more accurate beam spectra. A two-fold evaluation was performed for the two models by investigating the accuracy of the MC codes in water and that of the models in the exit dose plane under homogeneous and heterogeneous media. The two-fold evaluation was intended to distinguish the sources of error in the exit plane between MC codes and EPID models, offering better understanding of the performance of the EPID models. The evaluation of MC codes and MC models of EPID in the exit plane is necessary for the *in vivo* application of the MC models [19].

1.5Phase sorting method with dose reconstruction

For the actual, patient-specific dose calculation, there have been continuing effort to track the exact position of the tumor during the treatment [75]–[78]. If the tumor location is different between planning and treatment, the proposed dose reconstruction method in section 1.2 is not valid. Since current dose reconstruction methods are machine-oriented, main concerns are MLC

position, gantry angle and dose rate. However, for a realistic dose reconstruction, patient breathing motion should be considered. When CTV is degraded by the organ motion, larger PTV or gating or breath holding should be used [75]. Some researchers studied to determine exact position of the tumor during the respiratory motion by using marker implanted near the tumor location [76], [77]. However, when the breathing pattern is irregular, the breathing phase is not predictable and therefore organ at risk (OAR) sparing cannot achieved [78].

Other researchers suggested CT reconstruction methods from measured EPID images during the treatment to track a patient's inter-fractional anatomical change [79], [80]. However, these methods were limited when there was not sufficient angular information. Also, the reconstructed CT using EPID images with MV photons did not provide accurate density information as a kV-CT. Another group suggested intra-fractional tumor tracking method by combining kV-CBCT and EPID MV image [9] or MV tumor tracking from the acquired EPID image [81], but its application is limited to the calculation of tumor dose.

It is known that dose calculation on 4D CT is the most accurate for reducing errors related to patient breathing motion, unless a patient motion management technique is used [82]–[85]. Other methods to deliver desired dose to a patient accurately are respiratory gating or breath holding. However, those technique may allow slight displacement of the tumor from the targeted location [86]–[90]. Due to uncertainty of patient breathing pattern, it is still challenging to estimate how accurately the dose was delivered as planned. For patient with self-breath holding method, the tumor position has few millimeters variation among each holding step [86], [91], [92], which can be regarded as a different breathing phase in 4D CT. Also, tumor position may be shifted by intra-fractional or inter-fractional change of the patient. Therefore,

determination of the tumor position would solve this problem, where most effective when breath holding method is adopted.

Cai *et al.* introduced a 3D dose reconstruction method by phase determination using a 4D CT motion model [93] of a digital phantom. They assumed that any respiratory motion can be described by sum of basis displacement vector field of the respiratory motion. The acquired 2D projection images were compared with the reference image generated from 3D phantom and the phase was determined by iterative calculation method where the displacement vector field was minimized. They tested the method using the digital XCAT phantom; however, the method was not fully evaluated with a real phantom.

The aim of this study is to reconstruct dose from IMRT with free breathing motion. The acquired EPID images in cine mode during the treatment were phase-determined by comparing with predicted EPID images, and the dose to the patient during each breathing phase is reconstructed based on 4D CT images and summed over all phases. The suggested method in this study may enable clinicians to monitor accumulated dose from every fraction of the treatment. Also, it may be used as a reference to determine whether adaptation to the planning is required.

2. MATERIALS AND METHODS

This study is consisted of two parts. First, the previously developed EPID model [71] was modified by effective atomic number modeling to consider realistic Compton interaction in the EPID layers. Also, the penumbra profile was improved by adopting new phase space data generated by more realistic linac head modeling. As discussed above, the accuracy of the reconstructed dose is determined by the accuracy of the predicted EPID image. Jung *et al.* employed a convolution kernel to match the EPID image profiles [71]. However, if there is a steep dose gradient, the suggested method will lose the resolution of the image. In this study, the improved EPID model in XVMC was demonstrated and compared with the reference EPID model based on EGSnrc with virtual detector technique.

Second, the improved EPID model was used in 4D dose reconstruction with the phase sorting method to reconstruct actual received dose to the phantom. The phantom response function was generated from the Monte Carlo simulation and dose to the phantom was reconstructed from the acquired cine EPID images. The reconstructed result was compared with forward calculation for the evaluation of the accuracy of the predicted EPID image and the phase sorting method.

2.1EPID model simulation and evaluation

2.1.1 EPID model in EGSnrc

A Varian aS1000 EPID was modeled by employing a virtual detector algorithm[58], which is a fast voxelized portal image calculation method, in the EGSnrc MC code [74]. The new model is similar to the one that was previously developed by Siebers *et al.,* [58] but formatted into the EGSnrc code while allowing user inputs for all structural layers of EPID in terms of dimension, density, and elemental composition. The realistically modeled structures in this study included an air gap, a copper plate, a phosphor screen, back scattering layers, and other layers in EPID. The supporting arm was not modeled; backscattering influence was up to 5% in aS500 EPID [94] which was modeled in the virtual detector [58], but found to be insignificant for an aS1000 EPID model [64] used in this study. The EPID dose image was calculated in the phosphor layer which contributes to the EPID response predominantly with a linear response between the energy deposition in the phosphor and the pixel values of the EPID image [95], [96].

In order to perform calculation, the input photon source terms were prepared by generating 6 MV phase space files for various field sizes under the Varian linac head from the EGSnrc/BEAMnrc code [97]. The generated phase space files were then used to calculate exit fluence under various phantoms (phantom-phase space files) employed in this study. Finally, the calculated phantom-phase space files were used to calculate two-dimensional EPID dose images.

2.1.2 EPID improvement in XVMC code

The realistic structures of EPID employed in the EGSnrc could not be reproduced in the XVMC code, which defines structures by finite-sized uniform voxels composited of water-equivalent materials. Therefore, the thickness and elemental composition of each layer of EPID were alternatively modeled in the XVMC code. This was partly achieved by density scaling described in eq. (2) in the previous study [71].

$$\rho_{scaled} = \frac{1}{t}\sum_{i}(\rho_i \times t_i) \qquad (2)$$

where ρ_{scaled} and t are the scaled physical density and thickness of a layer in the model, respectively; ρ_i and t_i are the actual physical density and the thickness of an i-th physical layer of EPID, respectively. In the model, if the thicknesses of the layers were smaller than the dimension of the voxel, multiple layers as indicated by the index "i", comprised a single-voxel layer. In the current study, in addition to the previous scaling method, the elemental compositions of the structures were also considered to improve the model.

A probability of Compton interaction in a medium is proportional to its electron density (electrons/cm^3), which can be expressed by multiplication of the physical density (mass per unit volume) and the number of electrons per unit mass [99], [100]. The number of electrons per unit mass is proportional to Z/A, where Z and A are the atomic and the mass numbers of the medium, respectively. Since the number of electrons per unit mass of low-Z materials (Z/A of water = 1.40×10^{23}/g, bone = $1.4\sim1.5\times10^{23}$/g, lung = 1.46×10^{23}/g and soft tissue = 1.47×10^{23}/g) [100] are similar, the physical density-only scaling is acceptable for them. However, the number of

electrons per unit mass increases for higher-Z materials (Z/A of glass = 2.74×10^{23}/g, Copper = 2.77×10^{23}/g).

To model high-Z materials in the XVMC code, however, the value of *Z/A* relative to that of water should be considered in the scaling process. For each layer of EPID, the effective atomic number Z_{eff} was computed and then a normalized Z_{eff}/A value to that of water, noted as $Z^n_{eff}(E)$, was determined by the Auto-Z_{eff} software [101], which is reported as the most accurate method for higher energy (>10 keV) [102], considering the physics of Compton scattering in the layer for a given photon energy *E*. The average photon energy at 150 cm was determined from the exit fluence calculations performed in the section 2.1.1; it ranged between 1.7 and 1.8 MeV for 6 MV photon beams of varying field sizes of 5×5 cm^2 to 15×15 cm^2 that passed through phantoms of thicknesses of 10 to 30 cm. The calculated $Z^n_{eff,i}(E=1.75\ \text{MeV})$ of each (*i*-th) layer was then multiplied to the density ρ_i to determine the scaled effective density, $\rho_{eff,i}$ in eq. (3).

$$\rho_{eff,i} = \rho_i \times Z^n{}_{eff,i}\left(E = 1.75MeV\right) \tag{3}$$

By using $\rho_{eff,i}$, the Compton interactions in each layer was more physically modeled.

Applying the scaled effective density in eq. (2), a corrected effective density of a layer was derived in the EPID model in eq. (4),

$$\rho_{\text{scaled,Zeff}} = \frac{1}{t}\sum_i\left(\rho_{eff,i}\times t_i\right), \tag{4}$$

and used throughout this study. The performance of the corrected model was compared with that of the density-only scaled model developed previously [71].

In previous studies, it was found that the dose gradient in penumbra areas of simulated EPID images are smaller than that from measurements; the dose gradient across a heterogeneous interface was also smaller than those from measurements and EGSnrc calculations as well [43], [71]. The XVMC code used a virtual source model [103], which is composited by multiple sources with Gaussian spatial distribution in order to reduce calculation time. Therefore, it may not be physically accurate near field edges, since the virtual source model was optimized to water dose calculation near isocenter, without modeling the physical linac head structure. To improve the performance in the penumbra, the phase space files generated from the EGSnrc code in the section 2.1.1 were employed for the XVMC calculation. Similarly to the case of the EGSnrc model, the phantoms and field sizes were simulated to calculate EPID dose images in the phosphor layer of the XVMC model. While the calculations with the EGSnrc code involved multi-step process by using phase space data generated from previous steps, the calculations with the XVMC code involved only a one-step process of full 3D voxelized dose calculation from the phase space above phantoms to the EPID model.

2.1.3 Validation of the EPID models

One source of discrepancy between calculations and measurements could be attributed to the exit fluence accuracy in the plane of EPID that is governed by the fundamental physics model of the radiation transport through phantom and air gap layers of various thicknesses. In addition, they could be affected by potentially imprecise and/or inaccurate simulation due to limitations of the modeling of the actual structural and elemental composition of the EPID under

study. Therefore, the validation of the EPID models was separated into two steps: (1) validation of the codes with measured absolute doses to water in the plane of EPID under homogeneous and heterogeneous phantoms and (2) the validation of the EPID models with EPID measurements. The result of the second step contains the two sources of errors described above.

2.1.3.1 Dose to water in the plane of EPID: MC code validation

Doses were measured in an ion chamber array (PTW, Freiburg, Germany) that was placed under a 2 cm-thick buildup layer, including the inherent buildup, and above a 5 cm-thick backup phantom. The source-to-detector plane distance (SDD) was 150 cm. Photon beams with an energy of 6 MV from Varian Clinac iX, a dose of 200 MUs, and field sizes of 5×5, 10×10, and 15×15 cm^2 were irradiated through various phantoms to the array as shown in Figure 5. Since the IC array has a 1-cm resolution with the individual IC dimension of $0.5\times0.5\times0.5$ cm^3, the measurement was repeated after shifting the IC array diagonally by a half of the IC interspacing and merged the two measurements, doubling the resolution. The IC array was pre-calibrated to absolute dose at the isocenter and at the depth of 10 cm.

The phantoms included homogeneous and heterogeneous phantoms that were isocentrically placed as shown in Figure 5 (a) and (b), respectively. The former was homogeneous plastic water phantoms (CIRS, Inc., Norfolk, VA) of various thicknesses (10, 20, and 30 cm). The latter was constituted of a 3 cm-thick bone phantom or a 5 cm-thick lung phantom (Gammex, Inc., Middleton, WI) that were placed with their edges aligned to the beam

axis while being sandwiched between homogeneous plastic water phantoms. Detailed phantom thicknesses for the heterogeneous phantoms are listed in Table 1.

	Lung		Bone	
Total Thickness (cm)	15	25	13	23
upper water phantom	5.0	10.0	5.0	10.0
lung/bone phantom	5.0	5.0	3.0	3.0
lower water phantom	5.0	10.0	5.0	10.0

Table 1. Thickness configurations of the heterogeneous phantoms

Monte Carlo simulations were performed using the same conditions as the above setups. The phantoms of plastic water, lung, and bone used in the experiments were CT scanned and imported into the EGSnrc and the XVMC codes for the simulations. The dose calculation by the EGSnrc code in water was done by using the DOSXYZnrc user code [104]. The IC array with buildup and backup phantoms was replaced with a 7 cm-thick water phantom in the simulation and doses were calculated at a 2 cm depth. For comparison, the calculation voxel size was kept the same as the IC size ($0.5 \times 0.5 \times 0.5$ cm^3). The calculated doses by the two codes had been pre-calibrated to the absolute dose at the isocenter and at the depth of the dose maximum. The statistical uncertainty of the calculations was set to be within 0.2% on the value of the dose maximum. The calculation results were compared with the measurements.

The patient couch was not modeled in the simulation; instead, a measured couch attenuation factor was determined and applied to the simulation results.

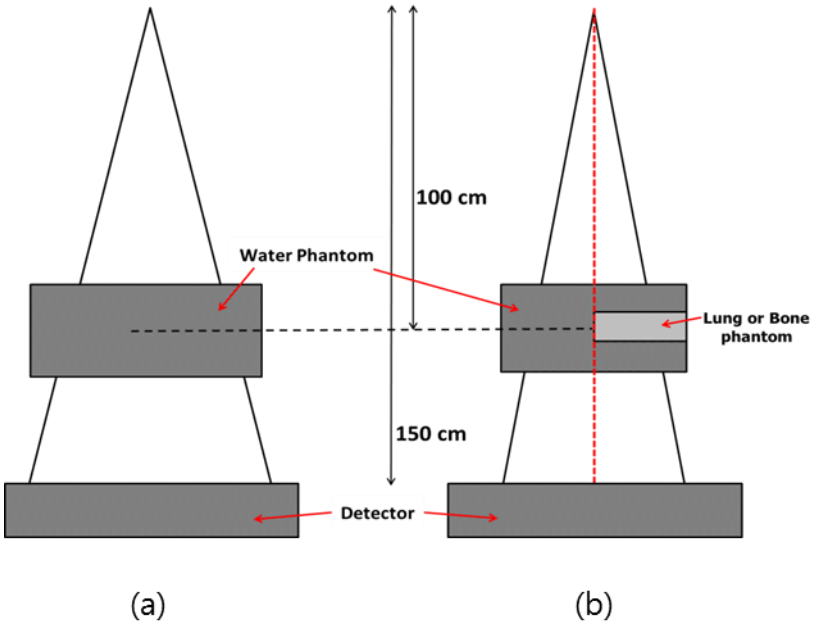

Figure 5. Experimental setups with (a) the homogeneous phantoms and (b) the heterogeneous phantoms. The phantoms were placed at the isocenter and the detectors (IC array or EPID) were placed at 150 cm. Phantom thicknesses were 10, 20, and 30 cm for the homogeneous phantom. The thicknesses of the lung and the bone phantoms were 5 and 3 cm, respectively. They were sandwiched by water phantoms of thicknesses of 5 and 10 cm.

2.1.3.2 Dose to the EPID:EPID model validation

Measurements of EPID dose images were performed for the same experimental conditions used in the dose-to-water measurements as shown in Figure 5. Prior to measurements,

the EPID was calibrated by dark field (DF) correction and gain correction. First, DF correction was performed for background noise cancelation by an EPID image acquired without radiation exposure. Since there was no external radiation, the EPID image should have null values at all points over the image; any measured value different from zero is considered as electrical noise and subtracted from the measured image. Second, gain correction was performed under irradiation with a uniform open field covering >70% of the EPID imaging plane. In this step, the sensitivity of each pixel was corrected by two-dimensional gain correction matrix under a 20 cm phantom to obtain a uniform image response [71].

The two-dimensional pixel-to-pixel calibration between the calculated EPID dose images and the measured images was performed under a 20 cm-thick phantom and the field size of 27.2×20.8 cm^2, which covers the imaging plane of the EPID. The calibration was then scaled to represent each condition of measurement, i.e. the field size of irradiation and phantom thickness, to provide a condition-dependent pixel-to-pixel calibration matrix. This is further explained in the result section. For the measurements, the integration mode of image acquisition, a dose of 200 MUs, and a dose rate of 300 MU/min were used.

For each of the experimental condition, the EPID image was also calculated on the MC models of EPID for comparative evaluations. The calculated images were then converted to measured images using the calibration matrix obtained above. In the EPID calculations, the patient couch was not modeled, because the couch was not modeled when the calibration matrix was generated. Therefore, neglecting the patient couch did not affect the final value of the converted images from the calculations. The pixel size of the calculations was 0.25×0.25 cm^2; the raw pixel size of EPID images was rescaled to the same with calculations for comparison.

For the XVMC model, the thickness of the phosphor layer was 0.25 cm, while it was actual thickness (in submillimeters) in the EGSnrc model.

2.2Four-dimensional dose reconstruction with the phase sorting method

A phase sorting method was developed for the determination of the phase of an object at which irradiation occurred. The method consists of forward calculation of cine EPID images through a moving object and correlation of measured cine EPID images during treatment with the calculated images, searching for, and thus determining the phase at the time of irradiation. A schematic flowchart of the method is shown in Figure 6.

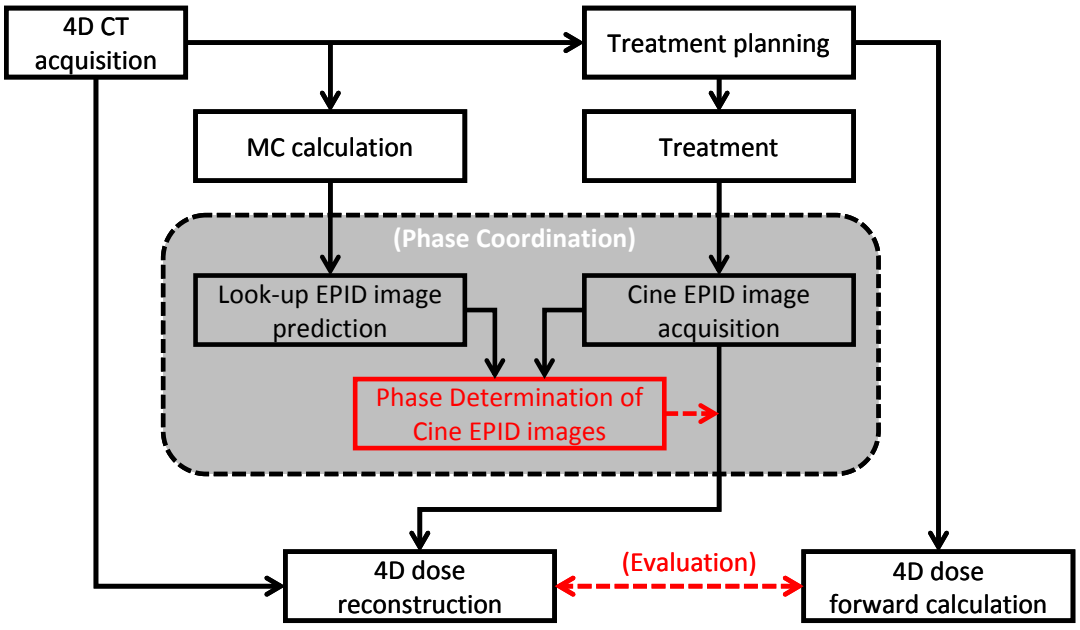

Figure 6. A workflow for 4D dose reconstruction with phase sorting method

2.2.1 Phantom configurations and EPID measurements

An in-house breathing motion phantom, representing a tumor within a lung, was developed. Polystyrene was used as the tumor material, and a cork was used as the lung material. The dimension of the polystyrene cylinder was 3 cm×3.5 cm (diameter×height), and the cork was 16.0×16.0×8.0 cm^3 (length×width×height), as shown in Figure 7. Whole phantom was placed on a moving platform that was moving back and forth with 2 cm amplitude and 4 sec/cycle in sinusoidal motion.

A Ten-phase 4D dynamic CT was taken for the moving phantom. For the cine EPID image measurement, a 6 MV photon beam with 300 MU/min using from Varian Clinac iX was irradiated on the phantom with three plans; (1) a static field with fixed jaw opening of 5.0×8.5 cm^2, (2) a dynamic field with maximum field size 10×10 cm^2, where MLCs close in parallel with the tumor movement (sliding windows), and (3) an IMRT field with MLCs open and then close in parallel with the tumor movement. Cine EPID images with 10 fps were acquired during the irradiations.

Also, to evaluate the phase sorting method, an anthropomorphic digital extended cardio-torso (XCAT) phantom with respiratory motion was used in this study [105], [106]. A tumor with 2 cm diameter was positioned in the lung (see Figure 8). The diaphragm motion was 2 cm and the breathing phase was 4 sec. A total of 5 phases of digital phantom were generated for the experiment. Detailed experimental condition will be described in section 2.2.4.

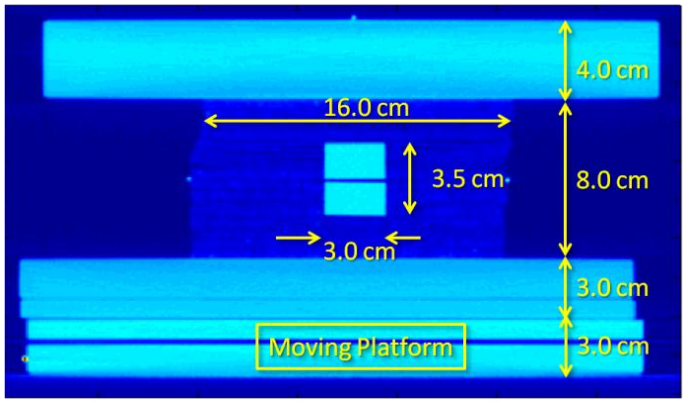

Figure 7. A cross-sectional CT image of the phantom. The phantom was home-made with cork and polystyrene. The lung phantom was sandwiched between water equivalent solid phantom and the entire phantom was placed on a sinusoidally moving platform.

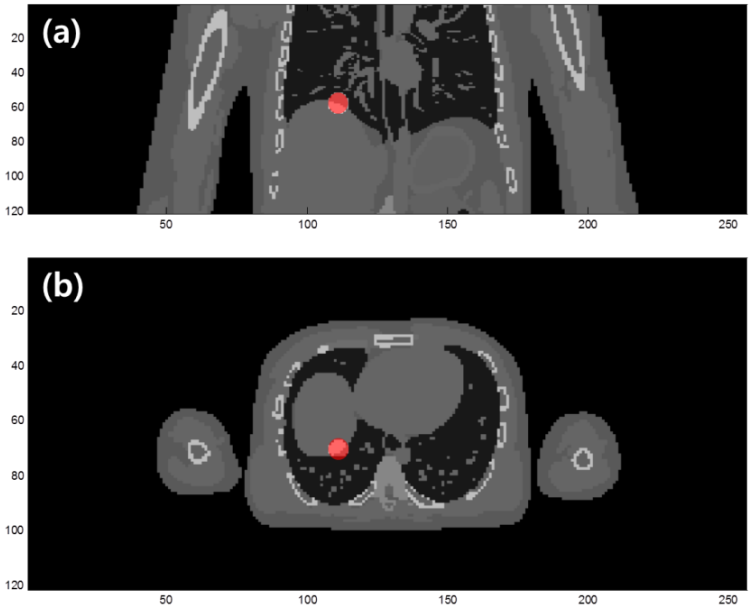

Figure 8. Cross-sectional images of the digital XCAT phantom. Respiratory phase 3 was shown with (a) coronal plane and (b) transversal plane view. The tumor was marked in red color in the figure. The resolution was (a) 3.125×1.563 mm^2 and (b) 3.125×3.125 mm^2, respectively.

2.2.2 Monte Carlo simulation: phantom dose

The phantom geometry was created for each breathing phase from the CT images. Then, EPID layers were attached under the phantom to calculate EPID dose images, as shown in Figure 9. The generated phantom with EPID layers was converted to XVMC input file format by in-house MATLAB code. Since XVMC calculates all doses to voxel in the volume geometry, forward calculation of phantom dose and EPID dose image prediction were done in a single calculation for each CT phase. In this study, the phantom geometries for maximum intensity projection (MIP; the intensity of a voxel is determined by the maximum value over all phases), average intensity projection (AIP; the intensity of a voxel is determined by the average value over all phases) and 4D CTs were created. It is known that the dose calculation on 4D CT is the most accurate [83], where the planning on AIP is better than MIP [107]. The doses were calculated for MIP, AIP and 4D CTs independently and compared with 4D forward and reconstructed dose.

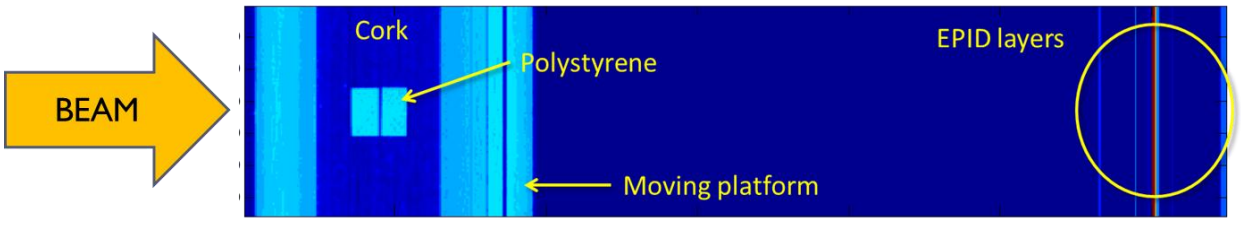

Figure 9. Cross-sectional view of the phantom geometry generated for the Monte Carlo simulation. The EPID layers were added to the CT image. The beam was irradiated from the left of the image.

2.2.3 Monte Carlo simulation: reference EPID image

Reference EPID images were calculated for the phase determination of measured EPID images with the same jaw openings as in the measurements, using the improved EPID model in this study by an enhanced layer modeling method and employing external phase space files generated from EGSnrc/BEAMnrc to improve outputs and penumbra shapes. The patient couch was not modeled in the Monte Carlo simulation; the error due to absence of the patient couch could be ignored since the acquired EPID images were converted into dose images by a simulated calibration image, and the effective thickness of the couch is very small relative to the phantom thickness in this study. The MLC shapes were not considered in the reference look-up EPID image simulations, since the phase had to be determined by the anatomical information of the patient, not the field shape. Also, the introduced 2D gamma method for the phase sorting calculates gamma index only within in-field regions; therefore absolute gamma values were not critical in the phase determination

2.2.4 Phase sorting of acquired cine EPID images

The measured cine EPID images were compared with pre-calculated look-up EPID images. Prior to the phase comparison, look-up EPID images corresponding to the reference phases were calculated by the Monte Carlo simulation using the phantom geometries generated from the 4D CT images. Also, pixel values on the measured cine EPID images were converted

into EPID dose image by normalization with a calibration EPID image simulated under a 20 cm thickness homogeneous phantom with the field size of 10x10 cm^2, as described in section 2.1.3.2.

The 2D gamma method [12] was used for the phase sorting. The gamma values were calculated by the equation

$$\Gamma = \sqrt{\frac{|r_r - r_m|^2}{\Delta r^2} + \frac{|D_r(r_r) - D_m(r_m)|^2}{\Delta D^2}} \quad (5)$$

where r_r and r_m refer to the evaluated distribution points on the look-up image at a reference phase and the measured image, respectively. $D_r(r_r)$ and $D_m(r_m)$ are corresponding value on the points. In the original gamma value calculation, $D_r(r_r)$ and $D_m(r_m)$ represent dose values on two-dimensional plane. In this study, the normalized pixel values on the EPID image were assumed as dose values for the purpose of comparison of EPID images. Δr and ΔD are distance to agreement (DTA) and dose difference (DD) criteria, respectively. In this study, 3 mm/3 % criteria was used for the gamma calculation.

Figure 10 shows schematic workflow of phase determination. To determine phase of a measured EPID image, gamma values were calculated by comparing with each phase of look-up EPID images. To avoid unnecessary calculation and error, only in-field region was considered in the gamma index calculation. Then, the phase of the EPID image was assigned to the reference phase where the sum of gamma values is lowest.

For dynamic or IMRT fields, the tumor could be temporarily shadowed by MLCs during the irradiation, which may cause inaccurate phase sorting results. In that case, the phases of

EPID images were correlated by interpolation or extrapolation in time frame, based on the sorted phases while it was available.

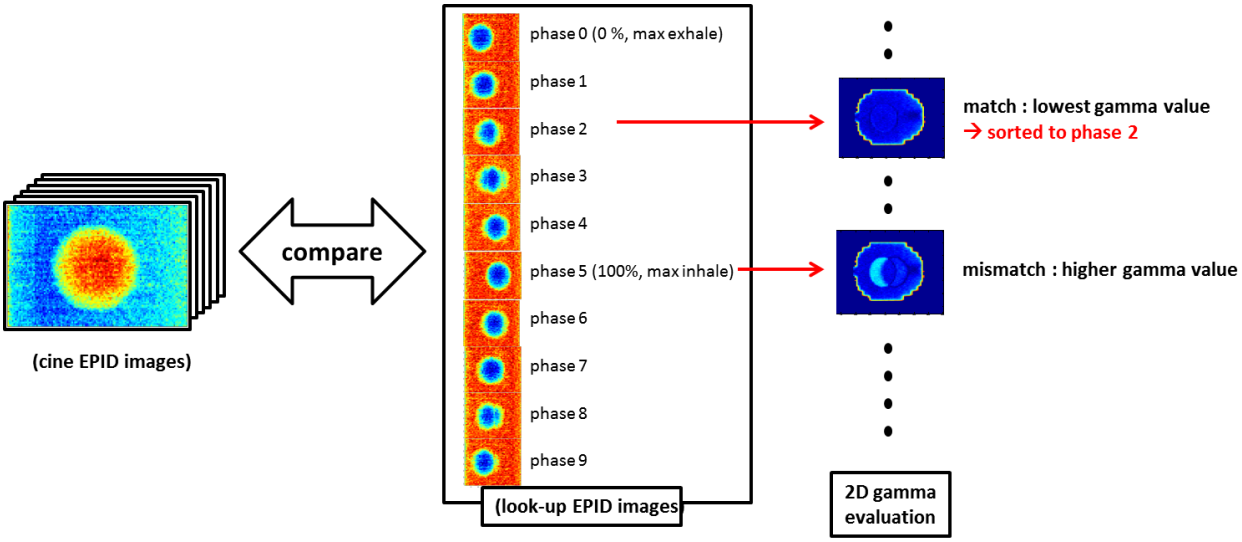

Figure 10. Schematic diagram of the phase sorting method. A measured EPID image was compared with look-up EPID images at the reference phases to determine phase of the image. The phase of measured EPID image was determined where the gamma value was lowest. In this example, the gamma value was lowest when compared with reference phase 2 and therefore the phase of measured EPID image was sorted.

Since the above phase sorting method utilized the rigid phantom, the method was also tested using deformable digital XCAT phantom with respiratory motion to evaluate the phase sorting method in a realistic case. The breathing motion was separated into five phases from maximum inhale to maximum exhale. Phantom images for each phase were generated and the phase 3 was chosen arbitrary as the reference phase. The EPID look-up images were simulated

for each phase from MC simulation with the improved EPID model in XVMC code. Since the phantom was in digital format, EPID image measurement was replaced by an MV digitally reconstructed radiographic (DRR) image calculated from XCAT model using projection image generation software included in the XCAT package. Field size of 15×7.5 cm^2 was used for MV image generation and look-up EPID image predictions. The generated MV image was compared with look-up EPID images and the phase was determined.

2.2.5 Dose reconstruction and evaluation

The dose was reconstructed from the phase-sorted acquired EPID images and corresponding 4D CT images by following steps. First, phantom response functions and EPID response functions for each reference phase were generated. Next, EPID-phantom relations were correlated using Eq. (1). Finally, phantom dose for a given phase was reconstructed inversely using the EPID-phantom relations. Detailed method was described in section 1.2. The reconstructed doses of each phase were transformed into the reference phase (reference exhale phase in this study) and summed over the volume. For the comparison, forwardly calculated 4D doses from the previous step were also transformed into the maximum exhale phase and summed over the volume for further evaluation.

The PTVs were determined on the acquired MIP, AIP and 4D CT images. Dose to PTV and lung were calculated forwardly on MIP, AIP and each phase of 4D CTs. Reconstructed DVHs for the PTV and lung were compared with forward calculation, MIP and AIP, respectively. Also, doses at the isoplane were compared by 2D gamma method.

3. RESULTS AND DISCUSSION

3.1Evaluation of EPID model in XVMC

The EPID modeling in MC codes were tested and compared with measurement. In this study, the EPID models in two MC codes (EGSnrc and XVMC) were tested. Since EGSnrc is known as the most accurate MC code for EBRT, the improved EPID model in XVMC code was also evaluated by comparing with the EGSnrc based model.

3.1.1 Dose to water in the plane of EPID: Monte Carlo code validation

For the MC code validation, doses were compared with the ion chamber measurement with SAD setup. The depths of measured points were 10, 20 and 30 cm and the field size was 10×10 cm^2. The solid water phantom was placed at the isocenter with more than 10 cm-thickness of back-scattering layer from the measurement point to provide sufficient scattering.

In this study, the XVMC code responded to IC measurements with the differences of +0.3, -0.1 and -0.3%, respectively, and the EGSnrc code responded with the differences of +0.8, +0.4, and +0.2%, respectively. The results were listed in Table 2.

Depth (cm)	XVMC	EGSnrc
10	0.3%	0.8%
20	-0.1%	0.4%
30	-0.3%	0.2%

Table 2.Dose difference of MC calculation from the IC measurement at the isocenter

3.1.1.1 Under homogeneous phantom

Absolute doses to water at the beam axis measured by the IC array and those calculated by the MC simulations were inter-compared for various phantom thicknesses and field sizes, as shown in Figure 11 (a) and Table 3. The couch attenuation was determined to be 2.3% with IC measurement, averaged over field sizes of 5×5 to 15×15 cm^2 and phantom thicknesses of 0 to 30 cm. The variation of the attenuation over the measurement conditions was less than 0.5%. This factor was applied to all dose-to-water calculations in this study. Table 3 showed that the maximum difference of the EGSnrc code was determined to be +2.8% for the field size of 5×5 cm^2 under phantom thicknesses of 10 and 20 cm and that of the XVMC code was +2.2% for the same field size under the 20 cm-thick phantom.

	Homogeneous Phantom Thickness							
Field Size	10 cm		20 cm		30 cm		Average	
(cm^2)	EGSnrc	XVMC	EGSnrc	XVMC	EGSnrc	XVMC	EGSnrc	XVMC
5 × 5	2.8%	1.7%	2.8%	2.2%	1.8%	1.3%	2.5%	1.7%
10 × 10	1.3%	1.0%	2.0%	1.4%	1.7%	0.5%	1.6%	1.0%
15 × 15	1.1%	0.7%	1.1%	0.4%	1.0%	0.4%	1.1%	0.5%
Average	1.7%	1.1%	1.9%	1.3%	1.5%	0.7%	1.7%	1.1%

Table 3. Differences between calculated doses by MC codes and measured doses in the IC array of irradiations through homogeneous phantoms at the beam axis in the EPID plane.

(a)

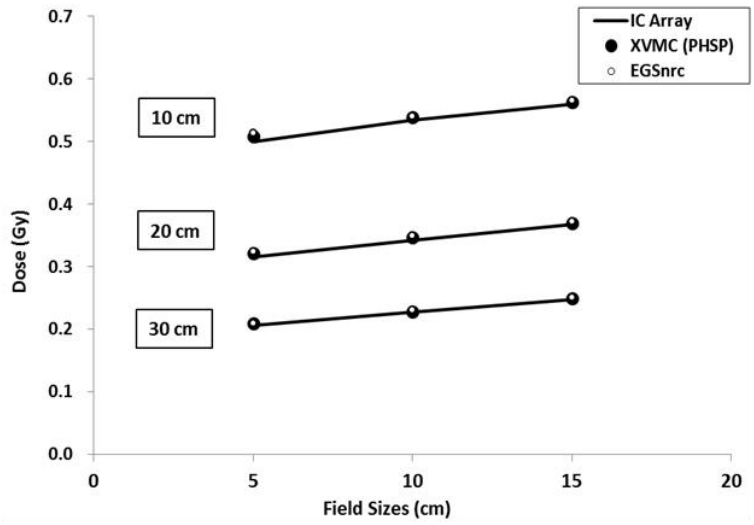

(b)

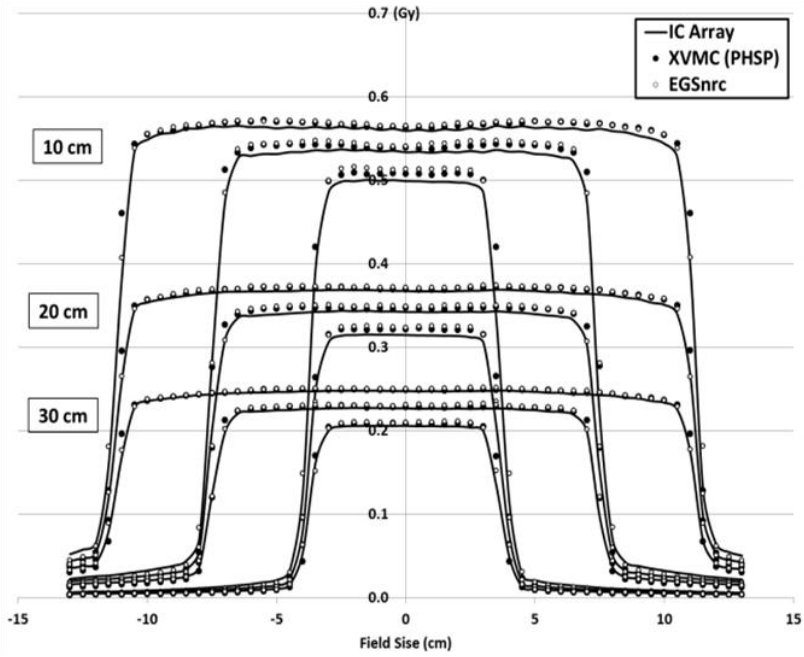

Figure 11. Inter-comparison of absolute dose to water by MC calculations and IC array measurements in the EPID plane under homogeneous phantoms. (a) Doses at the beam axis. (b) Off-axis dose profiles. Phantom thicknesses of 10, 20, and 30 cm and field sizes of 5×5, 10×10 and 15×15 cm^2 were used. Each graph displays results measured by ion chamber array, results calculated by the XVMC code (with the phase space source model), and results calculated by the EGSnrc/DOSXYZnrc code.

At the largest field size of 15×15 cm^2, both EGSnrc and XVMC codes provided the closest agreements for all phantom thicknesses. For the two codes, as the field size increased from 5 x 5 cm^2 to 15 x 15 cm^2, the calculated outputs relative to the IC outputs changed by greater than 1%, decreasing the MC over-response.

From the above differences in water dose at the isocenter, it was found that in the plane of EPID the two codes provided increased differences, as listed in Table 3, by producing greater relative responses to the ion chamber responses at the isocenter in Table 2. For example, the differences of +2.0% vs. +0.4% for the EGSnrc code and +1.4% vs. -0.1% for the XVMC code at the condition of a 20 cm thickness and 10×10 cm^2. In spite of the above variations, overall, the results of MC calculations showed small errors, less than the 2.8%.

As stated in the section 2.1.3, the MC accuracy is fundamentally influenced by the physics model of each code, which in turn affects the accuracy of the fluence at the level of EPID. It can be explained that the differences, found above and throughout this study, between the calculations and the measurements have been contributed by the level of such fundamental accuracy achievable by the MC codes, affected by the realized commissioning accuracy of them. As shown in the commissioning result, the output was decreased as the depth in the phantom increased; the same thickness effect was shown at the EPID plane. Therefore, it may be considered that higher response at the exit plane was due to the air gap, which yielded inaccurate scattering calculation in the air gap between the phantom placed at the isocenter and the EPID plane. However, the differences between the simulation results and the measurements agreed within less than 3%.

Off-axis profiles were inter-compared between calculations and measurements in Figure 11 (b). The average differences were acquired across the in-field regions (excluding penumbra area; 80% of FWHM) with a maximum standard deviation of 0.5% for all profiles throughout this study. Among the differences for all conditions, the maximum average differences (the maximum value among the average differences of each condition) were found to be 3.3 and 2.3% for the EGSnrc and XVMC codes, respectively, under the thickness of 20 cm and field size of 5×5 cm^2 as shown in Table 4. The maximum point differences (the maximum value among point maximums of each condition) were found to be 3.9 and 2.8% for the two codes, respectively, under the same condition. The maximum point differences were affected by proximity of their locations to high-dose-gradient regions (penumbra or heterogeneous interface) and MC noise in addition to the above fundamental reasons.

Calculated dose-to-water profiles by the XVMC code based on the virtual source and the phase space models were compared with the measurements from IC array placed at the EPID distance in Figure 12. A 20 cm-thickness phantom and the field size of 10×10 cm^2 were used. The phase space model provided a slightly better agreement in the in-field region and sharpened penumbra profiles. Note that the XVMC code with its inherent virtual source model is optimized for dose calculation in a water medium, and thus the virtual source model still provided a good agreement with measurements in water [103].

Irradiation Condition		Average Difference		Point Maximum	
Field Size (cm^2)	Phantom Thickness	XVMC	EGSnrc	XVMC	EGSnrc
5x5	10 cm	1.8%	3.0%	2.2%	3.4%
	20 cm	2.3%	3.3%	2.8%	3.9%
	30 cm	1.4%	2.3%	2.2%	3.0%
10x10	10 cm	1.3%	2.0%	2.1%	2.9%
	20 cm	1.5%	2.2%	2.2%	2.7%
	30 cm	1.0%	1.9%	1.9%	2.6%
15x15	10 cm	0.9%	1.2%	1.9%	2.1%
	20 cm	0.9%	1.3%	1.9%	2.1%
	30 cm	0.7%	1.2%	1.5%	1.9%

Table 4. Summary of differences across in-field regions in the plane of EPID between calculated doses by MC codes and measured doses in the IC array of irradiations through homogeneous phantoms.

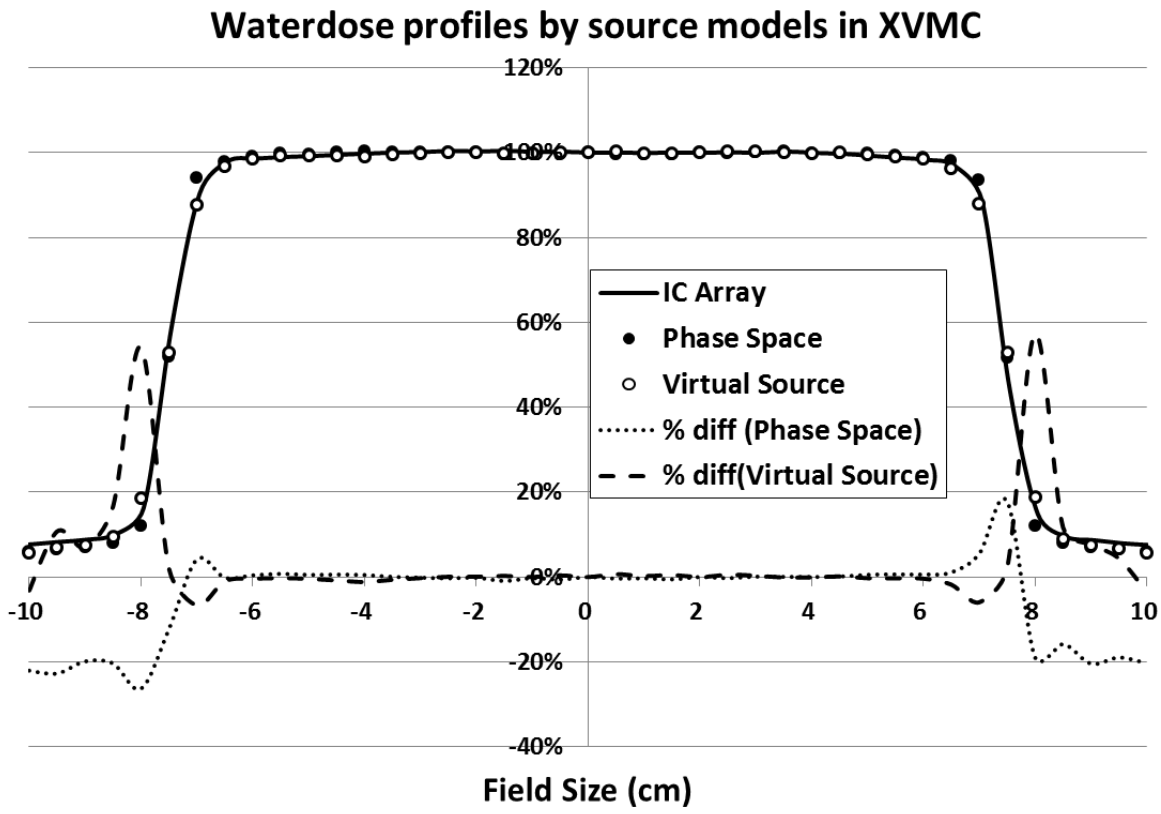

Figure 12. Inter-comparison of calculated dose-to-water profiles with phase space and virtual source models with reference to measurement by the ion chamber array. The experimental condition was under a 20 cm-thickness homogeneous phantom and the field size of 10×10 cm^2. The penumbra slope was slightly steeper when the phase space file was used.

3.1.1.2 Under heterogeneous phantoms

Absolute dose profiles under the heterogeneous phantoms are shown in Figure 13. The profiles are quantitatively evaluated in Table 5 in terms of average differences between the calculations and the measurements. The average differences were sampled across the in-field region (excluding penumbra and interface between water and lung/bone phantoms; 80% of

FWHM). The EGSnrc code yielded its maximum average difference of 2.9% under the bone phantom (in the water side) when the field size of 5×5 cm^2 and the total phantom thickness of 13 cm were used; the maximum point difference was 3.6% found in the same region under the same condition. The XVMC code yielded a maximum average difference of 2.3% and a maximum point difference of 2.7% in the same region under the same condition, where it was under the bone phantom.

	Field Size (cm^2)	Phantom Thickness	Maximum Average Difference				Maximum Point Difference			
			XVMC		EGSnrc		XVMC		EGSnrc	
Lung	5x5	15 cm	1.4%	(Water)	1.4%	(Water)	1.8%	(Water)	1.5%	-
		25 cm	1.7%	(Water)	1.4%	(Lung)	2.0%	(Water)	1.6%	(Water)
	10x10	15 cm	0.7%	(Water)	1.0%	(Lung)	2.3%	(Water)	1.7%	(Water)
		25 cm	0.9%	(Water)	0.9%	(Water)	2.1%	(Water)	1.6%	-
	15x15	15 cm	-0.9%	(Lung)	0.4%	(Water)	1.9%	(Water)	0.9%	(Water)
		25 cm	-0.7%	(Lung)	0.7%	(Water)	1.9%	(Water)	1.3%	(Lung)
Bone	5x5	13 cm	2.3%	(Bone)	2.9%	(Water)	2.7%	(Bone)	3.6%	(Water)
		23 cm	1.9%	(Bone)	2.6%	(Water)	2.4%	(Bone)	3.4%	(Water)
	10x10	13 cm	1.5%	(Bone)	1.8%	(Water)	2.5%	(Bone)	2.8%	(Water)
		23 cm	1.5%	(Bone)	1.9%	(Water)	1.9%	(Bone)	2.8%	(Water)
	15x15	13 cm	0.8%	(Bone)	0.7%	(Water)	1.9%	(Bone)	2.0%	(Water)
		23 cm	0.8%	(Bone)	0.8%	(Water)	2.1%	(Water)	1.8%	(Water)

Table 5. Summary of differences across in-field regions in the plane of EPID between calculated doses by MC codes and measured doses in the IC array of irradiations through heterogeneous phantoms. (Parenthesis represents the difference was found in which side of the phantom)

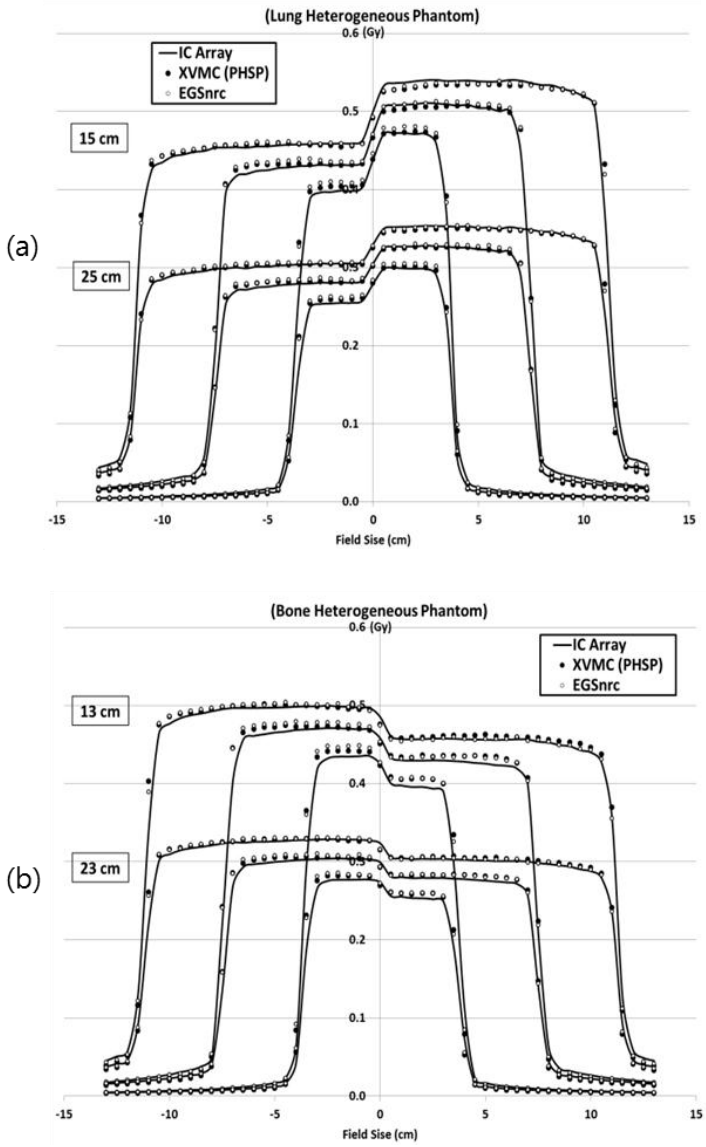

Figure 13. Inter-comparison of absolute dose-to-water profiles of MC calculations and IC array measurements across the EPID plane under heterogeneous (a) lung and (b) bone phantoms for field sizes of 5×5, 10×10 and 15×15 cm^2. Profiles for two sets of phantom thicknesses were provided in each graph. Each graph displays the profile measured by the ion chamber array, the profile calculated by the XVMC code and the profile calculated by the EGSnrc code. In each graph, the left half was under the water-equivalent phantoms and the right half was under the lung or bone sandwiched slabs.

Both EGSnrc and XVMC results showed the same field-size dependence as their performance in homogeneous phantoms: for all thicknesses, the error was largest for the smallest field size and decreased as the field size was increased.

Also, it was found that the average differences of the XVMC calculations are different between the lung and the water sides for all field sizes and thicknesses. This came from the fact that the relative outputs of the calculations to the IC outputs were smaller in the lung side than those under the water side. This finding is in contrast to the performance of the EGSnrc code that shows similar differences between the two sides, and thus the similar relative outputs for all field sizes and thicknesses. For example, for the XVMC code, under the 15-cm lung phantom and the field size of 10 x 10 cm^2 the difference on the lung side was -0.5%, compared with +0.7% for the difference on the water side; for the EGSnrc code, under the same condition these differences were +1.0% and +0.9%, respectively. This finding could be attributed to the limited accuracy reported for XVMC calculations in lung materials, compared with its performance in tissue-equivalent materials [72], affected by the commissioned accuracy of MC codes, discussed above. Overall, both XVMC and EGSnrc results showed good agreement with the IC array measurements within the maximum error of 3.6%.

3.1.2 Dose to EPID: EPID model validation

3.1.2.1 Under homogeneous phantoms

Figure 14 shows ratios of measured pixel values of EPID to calculated doses in the EPID models at the central axis. The ratios functioned as scale factors for dose-to-pixel value

conversions that are dependent on field sizes and phantom thicknesses in this study. In the figure, they were normalized at the condition of the field size of 10×10 cm^2 and the thickness of 20 cm at which two-dimensional dose-to-image calibration was performed. Across all thicknesses and field sizes, the ratios varied between 0.97 and 1.04 for the EGS model and between 0.92 and 1.07 for the XVMC model. With the smaller variation, the EGSnrc model performed more closely to the actual EPID, which can be explained by the better modeling achieved by incorporating the elemental compositions of the EPID structures. Both EPID models showed the same trend of the ratios: the measured pixel values/the calculated dose increased as the field size increased. This is similar to the trend of calculated dose/measured dose in water (Table 3 and Figure 11 (a)). However, the dependence of the ratios on field-size changes was much greater in the EPID models. In spite of the more realistic modeling of EPID as described above, the variance of the ratios implies deficiency in the accuracy of modeling, which could be related to the inaccuracy of elemental compositions available for EPID structures. The fact that the ratios increased with increasing field sizes and decreasing phantom thicknesses can be explained if the effective atomic number in the EGSnrc model is lower than the actual number. Low energy photons, which greatly interact with high atomic number materials, are more abundant as the field size increases and the phantom thickness decreases. A greater effective atomic number in the actual EPID caused its relatively higher response to the response of the EGSnrc model as the field-size increased and the phantom thickness decreased. The XVMC model, although it employed Z_{eff}, in principle could not experience low-energy over-response of high atomic number elements that are present in EPID. This explains a greater variation of the ratios. However, increasing Z_{eff} even higher than actual physical value would not enough to reduce the magnitude of ratios, since the hypersensitivity of the aSi EPID is mainly due to the phosphor layer [41], [42]. To overcome this

problem, energy kernel may be introduced to compensate for the energy dependency of the virtual detector model in EGSnrc code. For Z_{eff} corrected model in XVMC code, the dose calculation routine in the EPID layer may need to be modified.

Profiles of calculated dose images and measured images in EPID for various phantom thicknesses and field sizes were shown in Figure 15. The average difference of the EGSnrc model was 0.6% and the maximum point difference was 2.0% within the in-field regions as shown in Table 6 in spite of MC calculation noises for all conditions. The maximum average difference and the maximum point differences were found under the 30 cm-thick phantom and the field size of 5 x 5 cm^2. The average differences of the XVMC model were less than 0.4% and the point differences were less than 1.2% within the in-field regions for all conditions. They were found under the same condition above. The penumbra profiles of the two EPID models matched well to the measurements. The small differences came from the calibration based on the above ratios. Unlike the response of the MC codes in the plane of EPID, the performance of the EPID models were not affected by the dependence of their outputs on the changes of a field size and a phantom thickness or the increase of outputs in the EPID plane.

Irradiation Condition		Average Difference		Point Maximum	
Field Size (cm^2)	Phantom Thickness	XVMC	EGSnrc	XVMC	EGSnrc
5x5	10 cm	0.4%	0.5%	1.0%	1.3%
	20 cm	0.1%	0.3%	0.8%	0.7%
	30 cm	0.4%	0.6%	1.2%	2.0%
10x10	10 cm	0.2%	0.3%	1.2%	1.4%
	20 cm	0.4%	0.1%	1.1%	1.0%
	30 cm	0.1%	-0.1%	1.1%	-1.2%
15x15	10 cm	-0.3%	-0.1%	-1.2%	-0.7%
	20 cm	0.0%	-0.3%	-0.8%	-1.0%
	30 cm	-0.2%	-0.5%	1.1%	-1.7%

Table 6. Summary of differences across in-field regions in the plane of EPID between calculated doses by MC codes and measured doses in the EPID of irradiations through homogeneous phantoms.

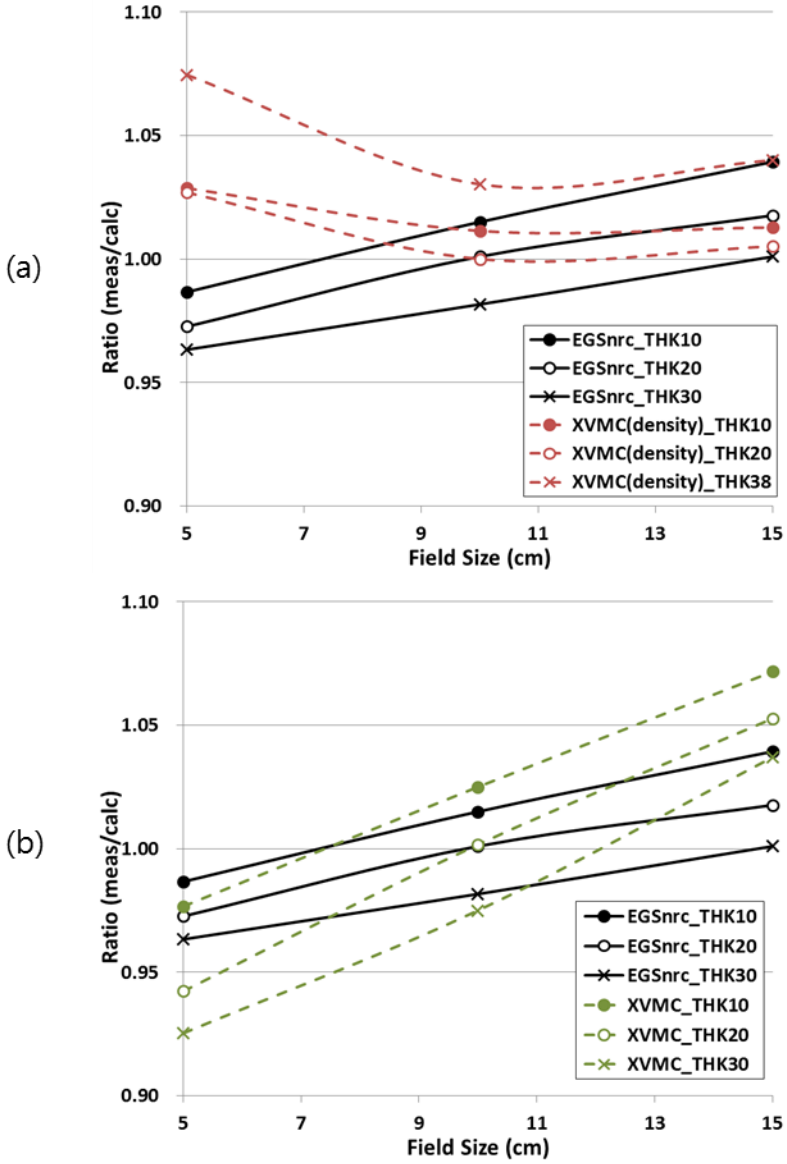

Figure 14. Ratios of measured pixel values of EPID to calculated dose in the (a) EGSnrc and XVMC (density scaled only) and (b) EGSnrc and XVMC (Z_{eff} and phase space correction) models of EPID as functions of field size and phantom thickness. The ratios were normalized at the field size of 10×10 cm^2 under a 20 cm-thick phantom. (Note that the maximum thickness used in density scaled model was 38 cm instead of 30 cm. The density scaled only data in (a) was reproduced from the previous study [71].

A noticeable change between the previous density-scaled XVMC model [71] and the new Z_{eff}-corrected XVMC model is that the ratios of the new model showed an increasing trend as field sizes increase, while the ratios of the previous model showed a minimum at an intermediate field size. The trend of the new model became similar to the trend of the EGSnrc model by considering Z_{eff}. This is encouraging because the outputs of the XVMC model simulated those of the actual EPID and the calibration factors (ratios in Figure 14) show a trend approaching linearity. This finding was not affected by the choice of the source models. In addition, an improvement in penumbra profile calculations was made as shown in Figure 16 by employing the phase space file from the EGSnrc code instead of the virtual source model used in the XVMC code. This change can be explained by the fact that the virtual source model is optimized for dose calculation in water equivalent or similar materials only [103], and thus is not suitable for modeling beam profiles measured in such heterogeneous media of EPID (compare Figure 16 with Figure 12).

All calculations in this study were performed by a computer equipped with dual 6 core 2.93 GHz Intel Xeon CPUs and 12 GB RAM. The total calculation time for the condition of a 20 cm-thick homogeneous phantom and the field size of 10×10 cm^2 was 1.2 hours for the XVMC model, while it took 14.9 hours for the EGSnrc model.

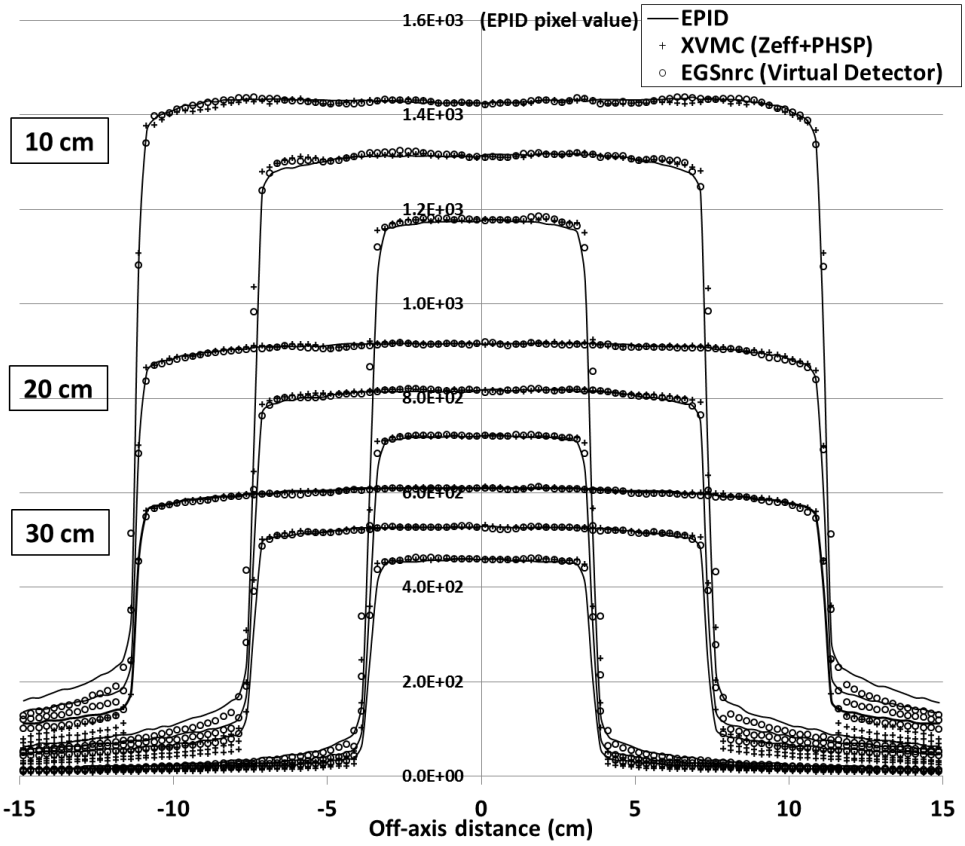

Figure 15. Inter-comparison of EPID image profiles by calculations in the EGSnrc and XVMC models of EPID and measurements in EPID under homogeneous phantoms. The phantom thicknesses of 10, 20, and 30 cm were used; the field sizes were 5×5, 10×10 and 15×15 cm^2. The XVMC model was calculated with the Z_{eff} structure model and the phase space source model. The EGSnrc model was calculated with the virtual detector model.

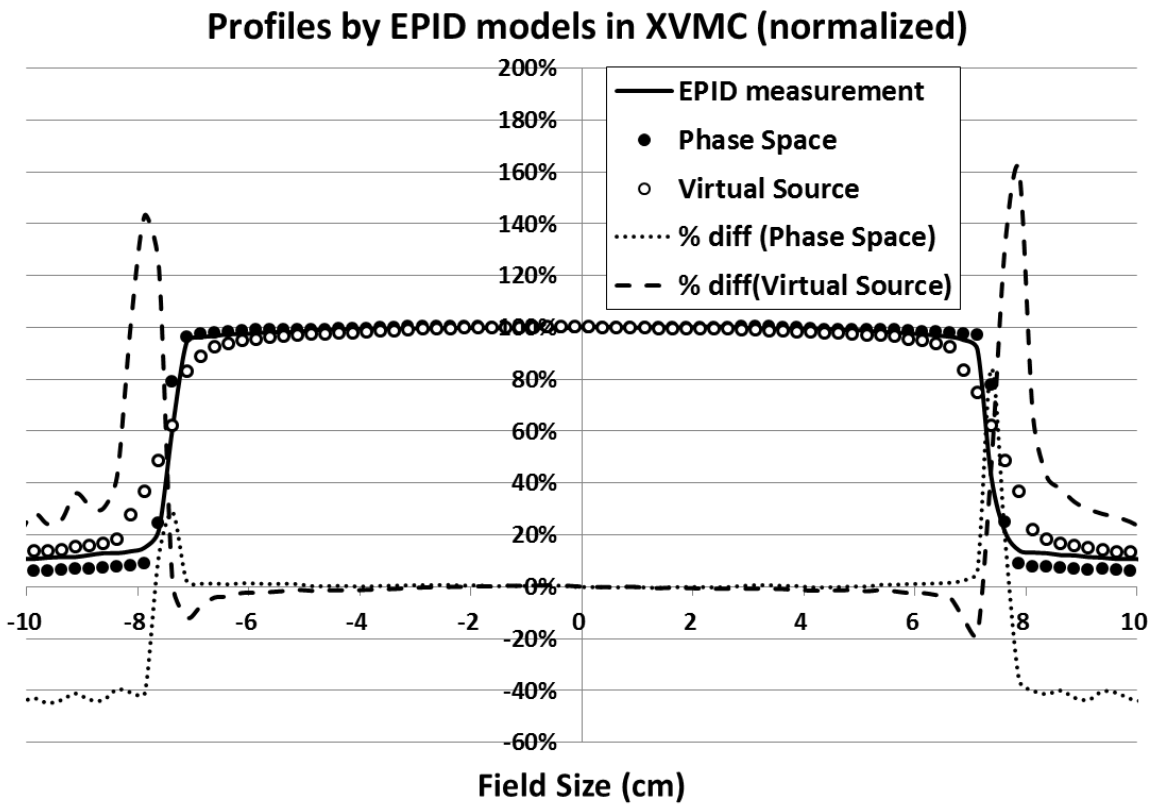

Figure 16. Inter-comparison of EPID image profiles calculated in the Z_{eff}–corrected XVMC model with the phase space and the virtual source models and measured in EPID for the field size of 10×10 cm^2 and a 20 cm-thick homogeneous phantom. The profiles were normalized at the beam axis.

3.1.2.2 Under heterogeneous phantoms

Calculated EPID dose images were similarly compared with measured images for the heterogeneous phantoms and field sizes described in the method section in Figure 17 and Table 7.

The comparison showed average differences less than 0.7% for the EGSnrc model for all conditions. The maximum was found under the lung side of the 15 cm-thick phantom with the field size of 15×15 cm^2. The maximum point difference was 1.4% under the same condition as shown in Table 7. The maximum average difference for the XVMC model was found to be 1.3% for the lung side of the 15 cm-thick phantom with the field size of 5×5 cm^2. The maximum point difference was 1.9% under the same condition.

	Field Size (cm^2)	Phantom Thickness	Maximum Average Difference				Maximum Point Difference			
			XVMC		EGSnrc		XVMC		EGSnrc	
Lung	5x5	15 cm	-1.3%	(Lung)	0.3%	(Water)	-1.9%	(Lung)	0.7%	(Lung)
		25 cm	-0.9%	(Lung)	0.1%	(Water)	-1.1%	(Lung)	-1.2%	(Water)
	10x10	15 cm	-1.0%	(Lung)	-0.2%	(Water)	-1.8%	(Lung)	1.3%	(Lung)
		25 cm	-0.5%	(Lung)	0.3%	(Lung)	-1.0%	(Lung)	1.1%	(Water)
	15x15	15 cm	-1.1%	(Lung)	0.7%	(Lung)	-1.7%	(Lung)	1.4%	(Lung)
		25 cm	-0.2%	(Lung)	0.3%	(Lung)	-0.6%	(Lung)	-1.2%	(Water)
Bone	5x5	13 cm	0.3%	(Water)	0.3%	(Water)	0.9%	(Bone)	-1.1%	(Water)
		23 cm	0.2%	(Bone)	0.3%	(Bone)	0.8%	(Bone)	0.9%	(Bone)
	10x10	13 cm	0.4%	(Bone)	0.2%	(Bone)	1.6%	(Bone)	-0.8%	(Water)
		23 cm	0.4%	(Water)	0.6%	(Bone)	1.7%	(Bone)	1.3%	(Bone)
	15x15	13 cm	-0.3%	(Water)	0.2%	(Bone)	-0.9%	(Water)	0.9%	(Bone)
		23 cm	0.0%	-	0.2%	(Water)	0.7%	(Bone)	1.0%	(Bone)

Table 7. Summary of differences across in-field regions in the plane of EPID between calculated doses by MC codes and measured doses in the EPID of irradiations through heterogeneous phantoms. (Parenthesis represents the difference was found in which side of the phantom)

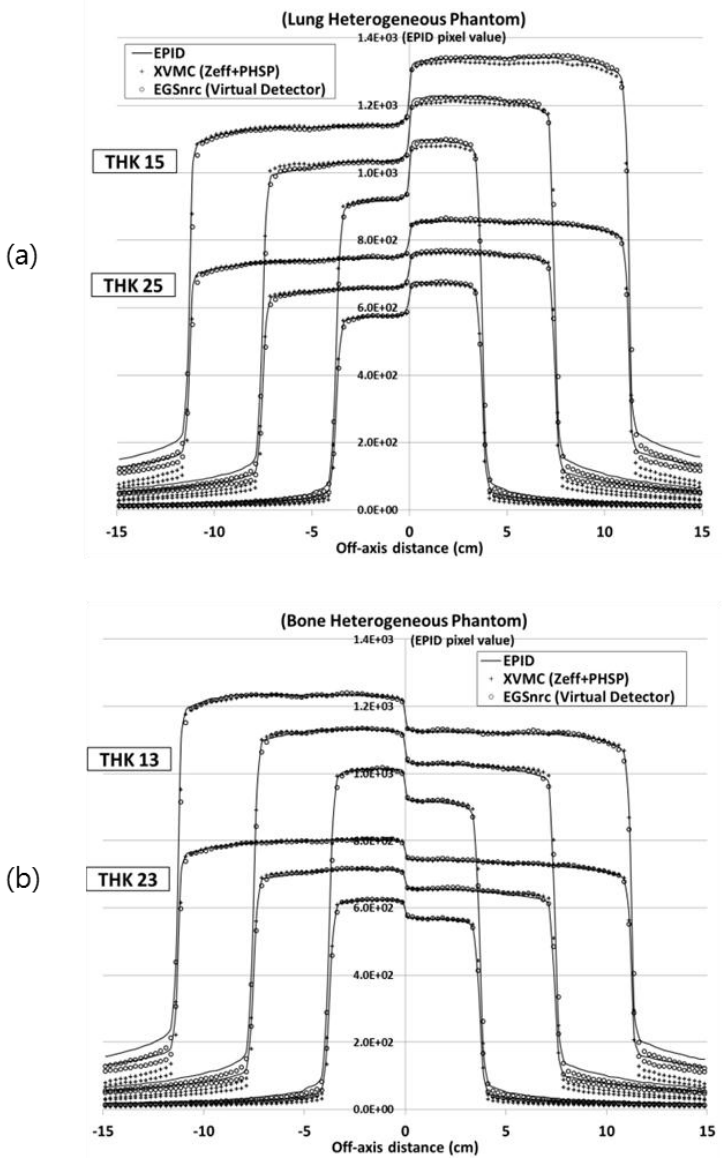

Figure 17. EPID image profile inter-comparison among the calculations of the EGSnrc and XVMC models and measurements under (a) heterogeneous lung and (b) bone phantoms for field sizes of 5×5, 10×10 and 15×15 cm^2. Profiles for two sets of phantom thicknesses were provided in each graph. In each graph, the left half was under the water-equivalent phantoms and the right half was under the lung or bone sandwiched slabs. Each graph displays the profile measured by EPID, the profile calculated by the XVMC EPID model (with the Z_{eff} structure model and phase space source model), and the profile calculated by the EGSnrc EPID model (with the virtual detector model).

Similar to the performance in the water phantom, the XVMC model produced different amounts of differences between the lung and the water sides for each field size and thickness, while the EGSnrc model produced similar amounts of differences as listed in Table 7. The differences of the XVMC model under the lung phantom were greater for the thinner phantom (15 cm-thick) than for the thicker phantom (25 cm-thick): of note, the differences were -1.3% vs. -0.9%, -1.0% vs. -0.5%, and -1.1% vs. -0.2% for the field sizes of 5x5, 10x10, and 15x15 cm^2, respectively. When it comes to the bone phantoms, there is no marked difference between the performances of the two models for each field size and thickness. These findings may be explained in the followings. The EPID images (i.e. pixel values) were obtained from calculated doses in the models through calibration that is dependent on field sizes and thicknesses of the water phantoms (not the lung/bone side). Therefore, greater differences were expected on the lung/bone side. This, however, did not have much impact on the results in Table 7, given the small differences between the effective thicknesses of the lung/bone side and those of the water side tried in this study. In support of this argument, the trend of data (differences under the lung/bone phantoms compared with those under the water phantoms for the two codes) in Table 5 appeared to be extended to that in Table 7 with one exception, the XVMC model under the 25 cm lung phantom and the field size of 15 x 15 cm^2. Thus, the trend of the above data was contributed mainly by the performance of the two codes, affected by the fundamental MC accuracy discussed above and secondarily by the calibration adopted in this study. Note that this argument is applicable to the level of heterogeneity of phantoms tried in this study; in reality, the effective thicknesses in patients could be more variable.

As shown in Table 7, the maximum average differences and the maximum point differences were reduced from the calculations in water to the calculations in the EPID models for all conditions of field sizes and thicknesses (compare 3.3% for the EGSnrc code with 0.7% for the EGSnrc model; compare 2.3% for the XVMC code with 1.3% for the XVMC model). Also, although the EGSnrc code was associated with a greater difference in water than the difference of the XVMC code for all conditions of field sizes and thicknesses, it was with a smaller difference in the model. This change was achieved by the calibration adopted in this study and the fact that the EGSnrc model is associated with a smaller variation of the ratios for the calibration than that of the XVMC model.

3.2Four-dimensional dose reconstruction with the phase sorting method

3.2.1 Phase sorting results

The phases at acquired EPID images were determined by 2D gamma comparison method. The tumor locations and corresponding EPID images were shown in Figure 18. In the diagram, phase 0 was max-exhale and phase 5 was max-inhale. Since the breathing motion in this experiment was sinusoidal, the phase at the same amplitude (displacement from the one end of the motion) cannot be distinguished whether it was during inhale or exhale motion. For example, the location of phase 1 was the same to that of phase 9, and phase 2 was the same to phase 8, etc. As a result, some reference phases were not used as a result of the phase sorting.

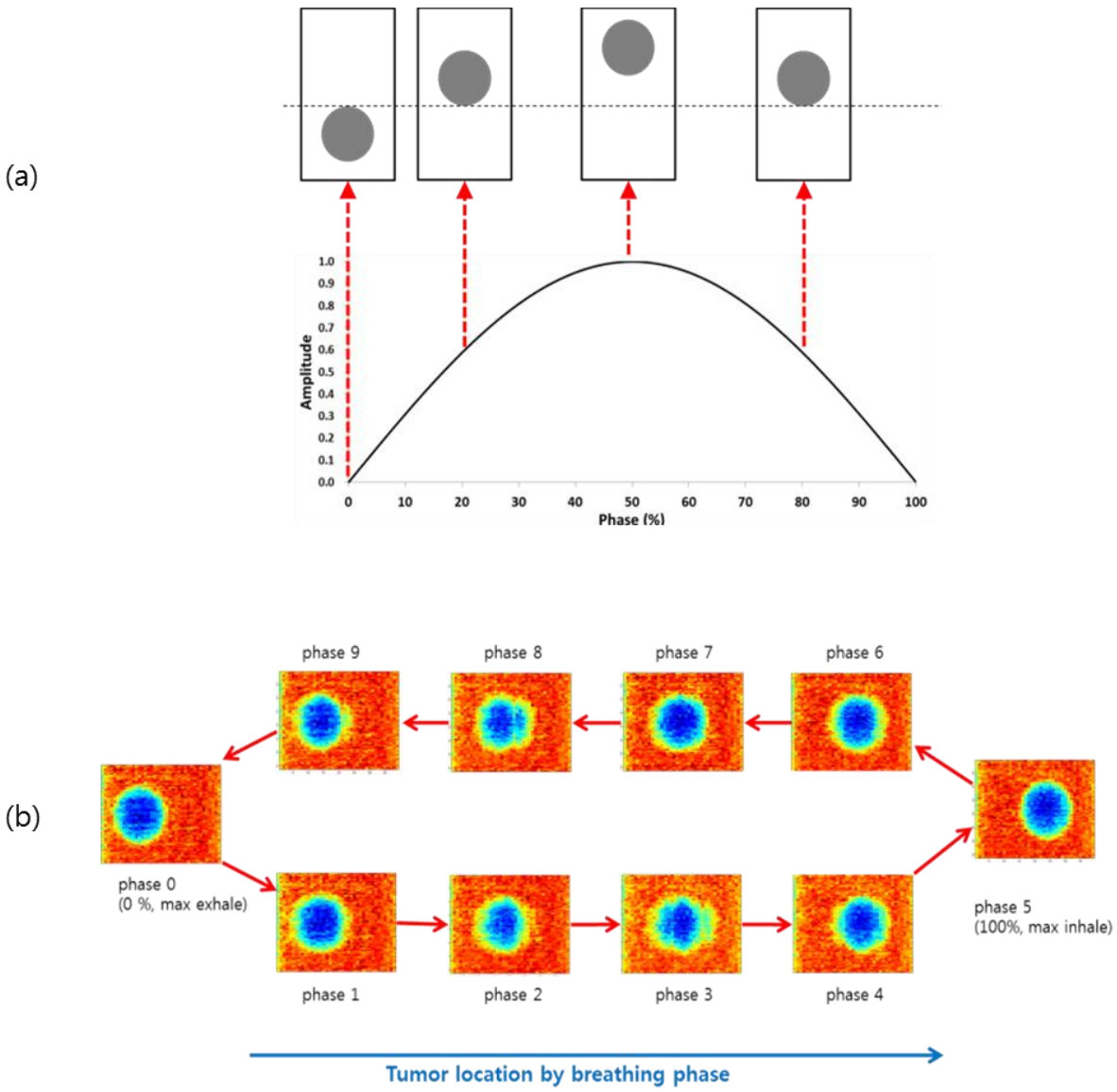

Figure 18. Look-up EPID images for sinusoidal breathing motion. (a) Simplified patient's breathing phase and corresponding EPID images by phase was shown. EPID images at phase 2 and 8 are the same. (b) Simulation result of look-up EPID images by reference phase from 4D CTs. (Note; the images used in (b) are predicted EPID images from a 4D CT set. The artifacts in the images (phase 3, 8, 9) were resulted from 4D CT motion artifacts.)

The 2D gamma values were calculated between a measured EPID image and a look-up EPID image at a reference frame, as shown in Figure 19. Note that the gamma criteria or absolute pass rate are meaningless in this comparison, since the purpose of this comparison is to find out the closest look-up EPID image from the measured image. The sorted phases were shown in Figure 20. Since the amplitude of the breathing motion is symmetry for inhalation and exhalation, only phase 0~5 were used for the phase sorting. Some images were sorted in adjacent phase of the predictions which were determined from the phantom motion; this could be due to a slight misalign of the experiment or motion blurring [108] of the 4D CT images. For the EPID images when the tumor was shadowed by MLCs, the phase was assigned manually based on the phase sorted result when the tumor was visible. For frame number 50 to 70 in sliding window, the tumor was half-shadowed by the MLCs and the phase sorting result was coincident to the manual sorting result. After then, the tumor was completely covered by the MLCs and the manual sorting method was used.

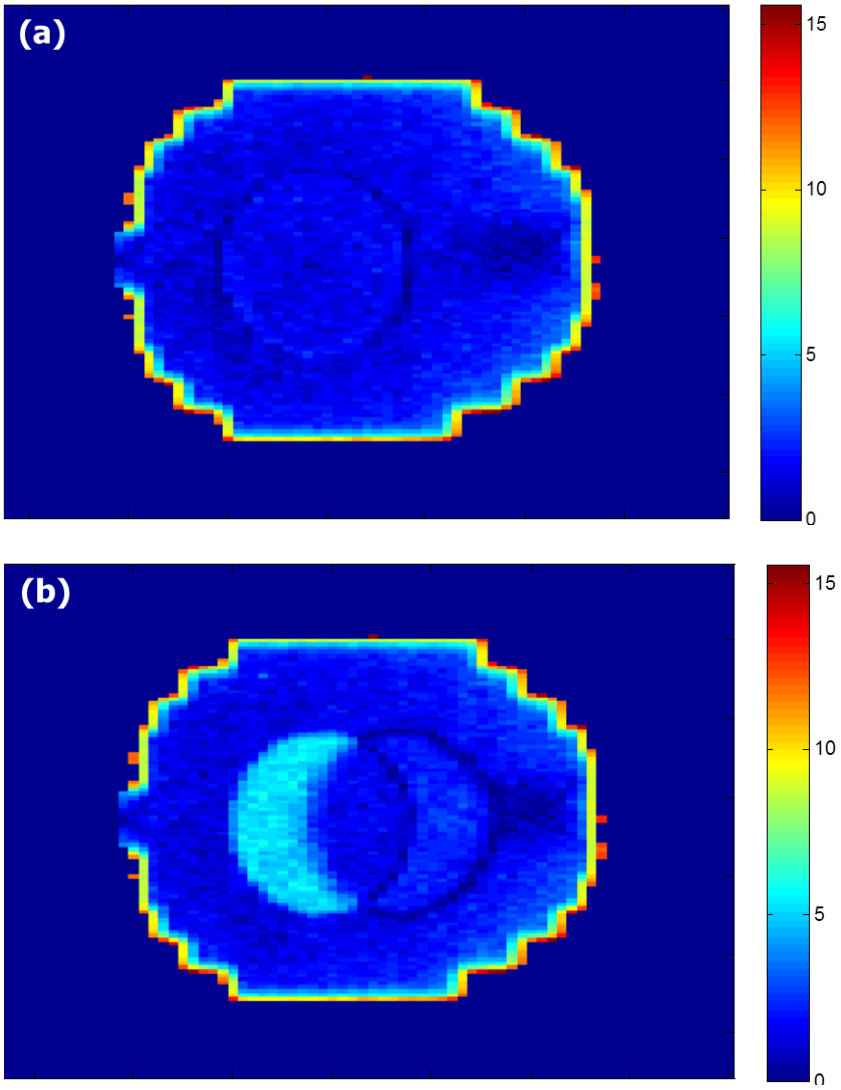

Figure 19. Examples of 2D gamma comparison result for the phase sorting. The results from IMRT field were shown. The pictures show 2D gamma map for a measured phase when a reference phase of look-up EPID images was (a) matched and (b) mismatched. The sum of gamma indices was lower for (a) and the phase was determined accordingly. The gamma values were calculated only for in-field (threshold 15% of maximum pixel value)

(a)

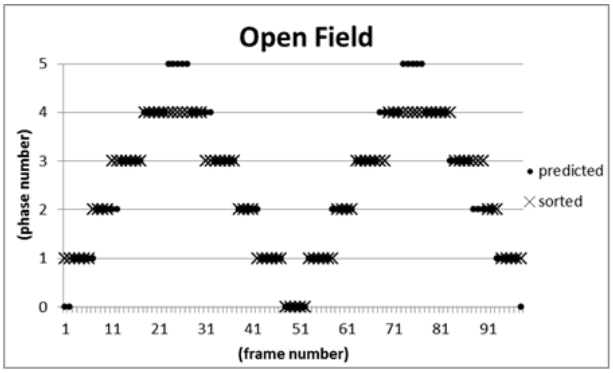

(b)

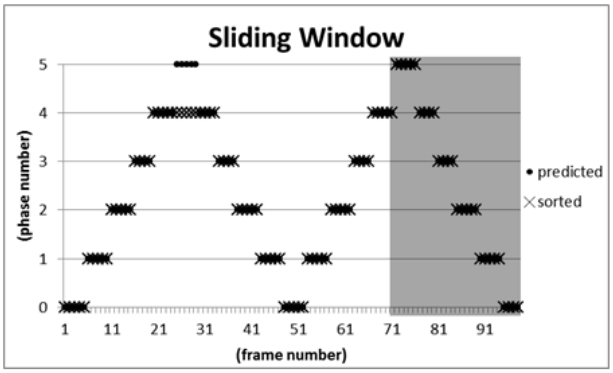

(c)

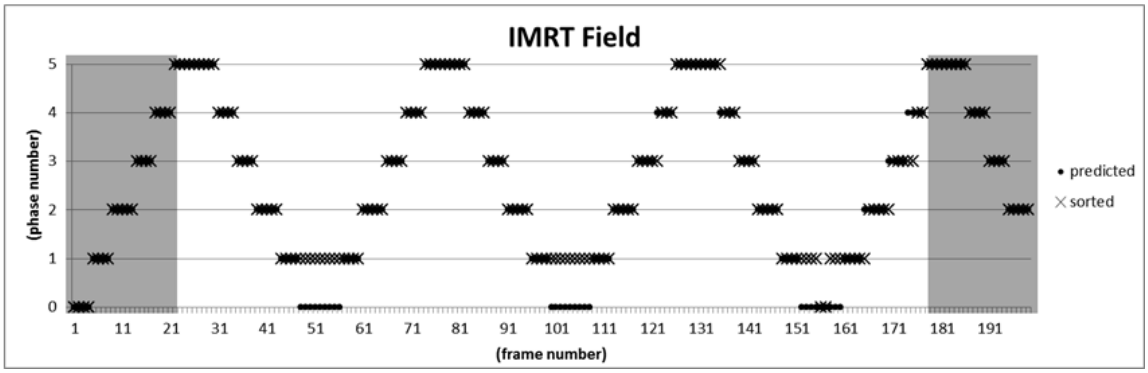

Figure 20. Sorted phase numbers of acquired EPID images and the predicted phase by phantom motion for (a) open field, (b) sliding window and (c) IMRT field. Phase 0 and 5 were longer than others since they were max-exhale and max-inhale, respectively. Frames where the tumor was hidden by MLCs were represented (shadow box) in the graph.

3.2.2 Reconstructed dose evaluations

The phantom doses were reconstructed from the sorted EPID images. The reconstructed doses were compared with forward calculations on MIP, AIP and 4D CT by DVHs and 2D dose at the isoplane. The result for the open field was shown in Figure 21. In the figure, "4D plan" (forward calculation) and "Reconstructed" were compared. Greater dose differences and gamma values are found near the edge of the tumor than the values in other areas on the coronal isocentric plane, as shown in Figure 21 (c) and (d), respectively. This was affected by the phase misalignment of the cine images discussed in section 3.2.1. Gamma pass rate was 92.7% for the 3%/3mm criteria, where the failure points were mainly at the tumor boundary. DVHs on AIP and MIP were higher than 4D doses and they showed very similar curve. Also, 4D forward and reconstructed doses were in good agreement. The evaluation of DVHs shows that the 4D reconstruction was performed accurately enough to cause close agreement between the "Reconstructed" with the "4D planed." The 3D dose calculations ("Planned" - both MIP and AIP) showed a greater DVH trends in PTV than the other two. This implies that the 3D dose calculation performed on an image of a moving target with margins of the internal motion and the setup uncertainty conservatively estimated dose, compared with the realistic "4D plan." The fact that the DVHs of the "Planned" were greater was likely resulted from the relative low dose coverage of the 4D cases when the locations of the tumor were closer to the boundaries of the irradiated field. The 3D dose calculations also showed different DVH trends in lung, overestimating volume coverage in high dose regions. This can be in part explained by the presence of greater lung volumes in 4D dose calculation than those in 3D dose calculation which employed MIP in this study.

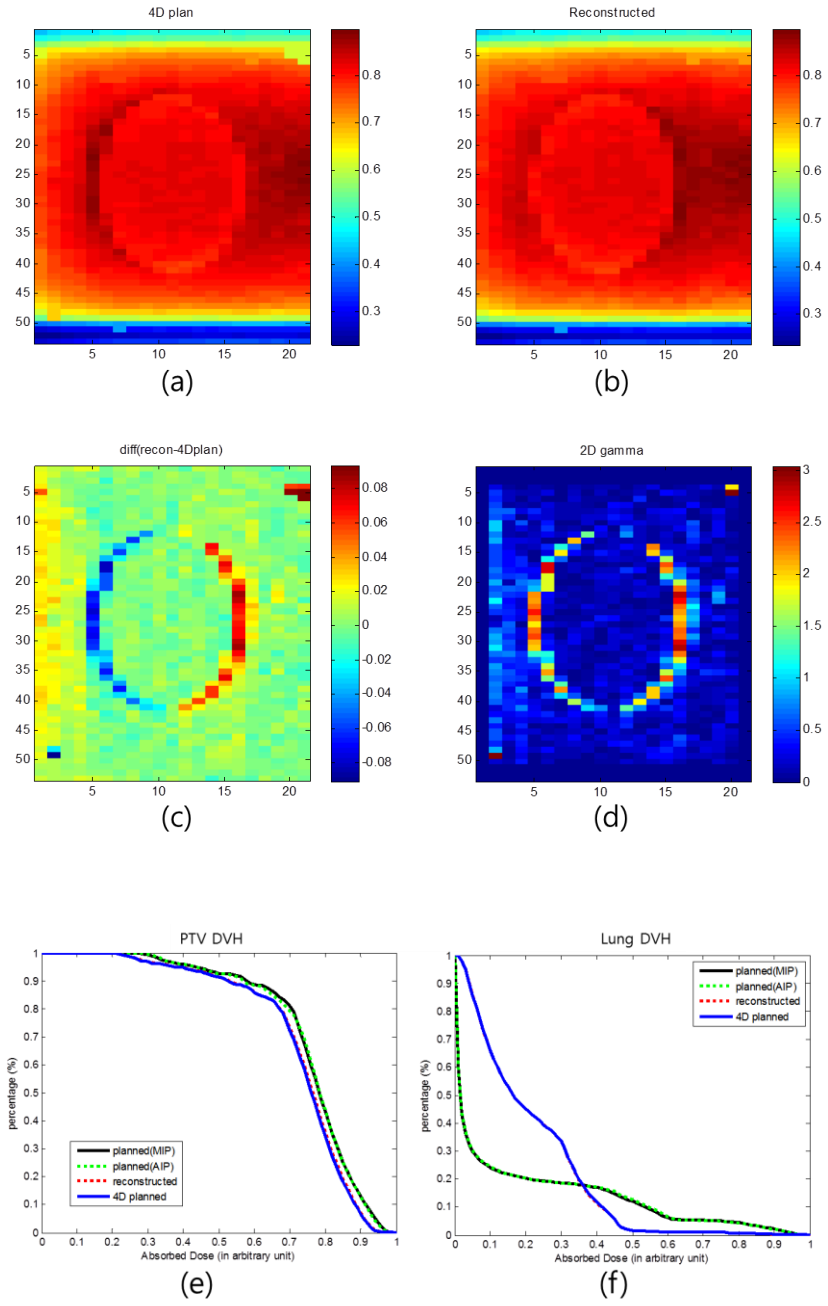

Figure 21. Dose distributions on the coronal isocentric plane for the open beam. (a) Planned dose on 4D CT image, (b) reconstructed dose by the phase determination method, (c) difference between planned and reconstructed dose, and (d) 2D gamma map. 2D gamma pass rate was 92.7% for 3%/3mm criteria. (e) DVHs in PTV of forwardly calculated doses on MIP and 4D CTs, and reconstructed 4D dose. (f) DVHs in lung. (The resolution of (a)-(d) was 2.5×1.0 mm^2)

The result for the sliding window was shown in Figure 22. Similarly, “4D plan” and “Reconstructed” were compared. Although not as obvious as Figure 6, greater dose differences and gamma values are found near the edge of the tumor than the values in other areas on the coronal isocentric plane, as shown in Figure 22 (c) and (d), respectively. The higher gamma values were found near the edges of MLCs that moved which was synchronized with the phantom motion during irradiation as shown in Figure 22 (d). DVHs of static volume were lower than 4D for the same region. The gamma pass rate was 100.0% for 3%/3mm criteria, where it was decreased 91.6% when 1%/1mm criteria were applied. It was greater than the result of the open beam, due to smoother variation of the dose, near the target edges, that tends to lower gamma value. In addition to the high gamma pass rate, the evaluation of DVHs shows that the 4D reconstruction was performed accurately enough to cause close agreement between the “Reconstructed” with the “4D plan.” The “Planned” on MIP and AIP showed smaller DVH trends in PTV as well as lung than the 4D dose. This could be affected by the greater portions of the PTV and the lung blocked by the moving MLCs during irradiation, while the planning CT image was stationary, than those of the 4D cases. The DVHs for MIP and AIP showed a straight line since the MLCs were moving with a constant speed, where 4D doses were curved due to partial exposure on the tumor during the tumor-MLCs interplay. Also, the DVHs for MIP and AIP showed a monotonic curve in lung. The trend of the “4D plan” and “Reconstructed” showed differences from “Planned”, due to modeling of partial exposures on the tumor that occurred during irradiation.

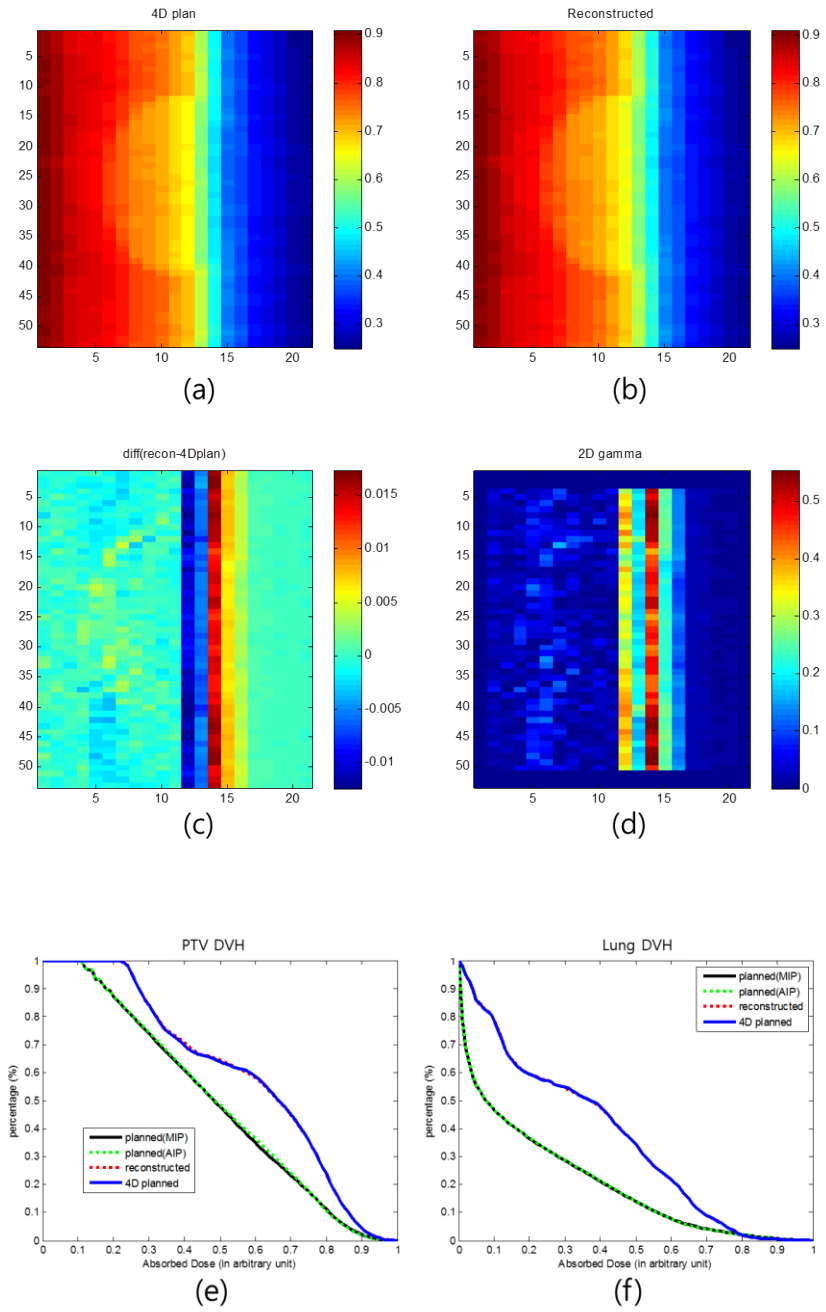

Figure 22. Dose distributions on the isocenter plane for the dynamic beam. (a) Planned dose on 4D CT image, (b) reconstructed dose by the phase determination method, (c) difference between planned and reconstructed dose. (d) 2D gamma map. 2D gamma pass rate was 100% for 3%/3mm criteria. (e) DVHs in PTV for forwardly calculated doses on MIP and 4D CTs, and reconstructed 4D dose. (f) DVHs in lung. (The resolution of (a)-(d) was 2.5×1.0 mm^2)

Figure 23 shows the result of the IMRT field. The MLCs were closed at the beginning, then opened widely and finally closed. The MLCs moving direction was same to the tumor motion. DVHs of 4D doses ("4D plan" and "Reconstructed") had better coverage than DVHs of static volume due to the synchronization between MLCs and phantom movement. Gamma pass rate was 98.1% for 3%/3mm criteria. It was lower than sliding window but higher than open field, since the phase mismatching appeared in the open field case was not observed in the IMRT field, as shown in Figure 20. The accurate performance of the 4D reconstruction was repeated, showing close agreement between the "Reconstructed" with the "4D plan." Similarly to Figure 22, "Planned (MIP)" and "Planned (AIP)" showed smaller DVH trends in PTV as well as lung than the other two.

While the agreement between the "Reconstructed" and the "4D plan" was encouraging, the small extent of differences between them, as shown in Figures 21(c), 22(c) and 23(c), came from multiple factors. First, as explained above, the phase mismatching played a major role. Second, the inverse 4D dose reconstruction algorithm used in this study does not employ segment-specific dose response calculations, but virtual beam let calculations from open fields that are slightly greater than the largest IMRT fields. The forward 4D dose calculation on the other hand employed segment-specific dose calculations. Third, since the displacement of tumor locations between phases (1.9 mm) near maximum inhale/exhale in this experiment is smaller than the CT slice thickness (2.5 mm), it is vulnerable to be sorted in adjacent phase. In spite of the above constraints, the generous tolerance of the gamma test (3% and 3 mm) and the cumulative nature of DVH did not show serious disagreement.

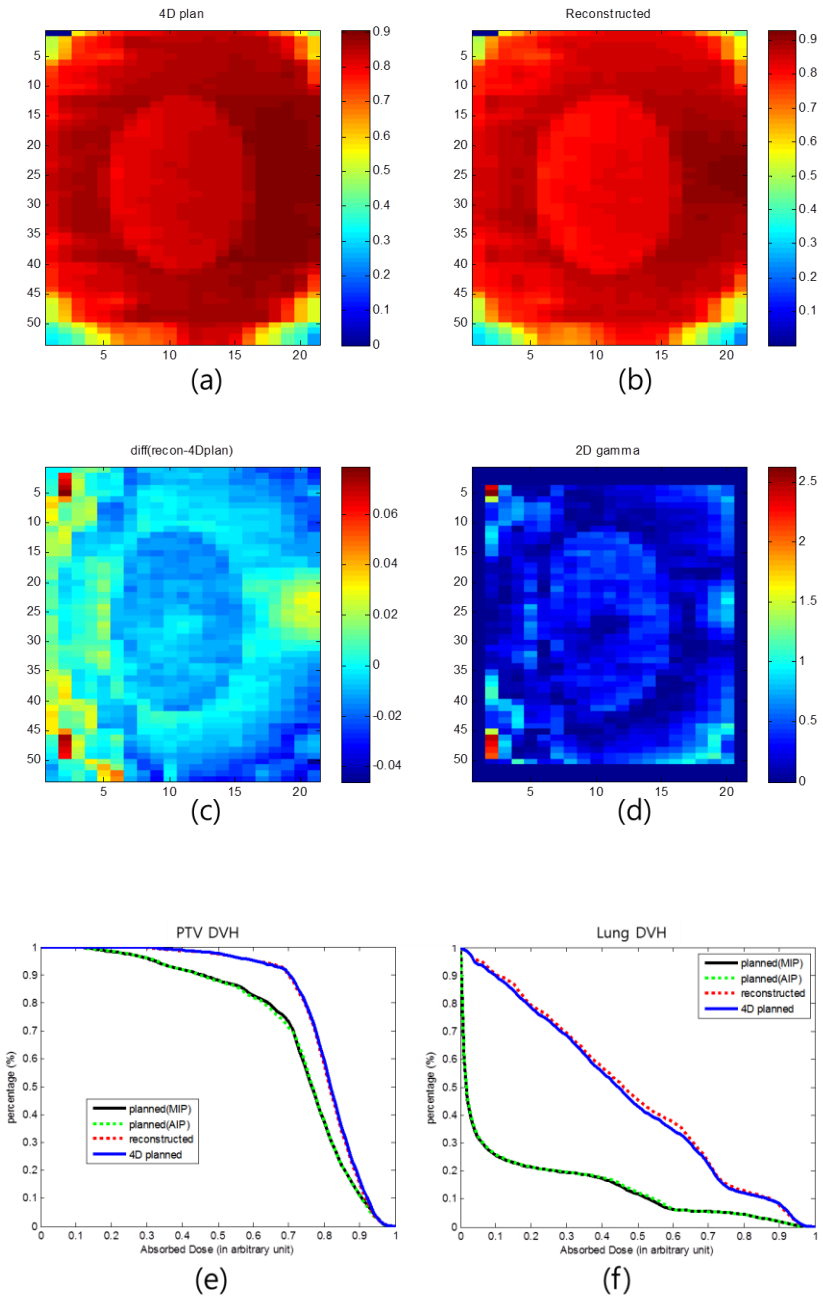

Figure 23. Dose distributions on the isocenter plane for the IMRT beam. (a) Planned dose on 4D CT image, (b) reconstructed dose by the phase determination method, (c) difference between planned and reconstructed dose. (d) 2D gamma map. 2D gamma pass rate was 98.1% for 3%/3mm criteria. (e) DVHs in PTV for forwardly calculated doses on MIP and 4D CTs, and reconstructed 4D dose. (f) DVHs in lung. (The resolution of (a)-(d) was 2.5×1.0 mm^2)

3.2.3 Phase sorting method evaluation: XCAT phantom test

To evaluate the presented phase sorting method using 2D gamma values in a realistic case, the generated MV DRR from the XCAT software package was treated as a measured EPID image in this experiment. Since the DRR image response is different from that of EPID image, there was mismatch in intensity of pixels after calibration due to difference in energy response of the EPID. However, since the phase sorting method utilizes the summed gamma values, the discrepancy of the pixel values would not affect the sorted phase. Since the dose reconstruction was not performed in this test, the pixel values were normalized to unity for ease of gamma comparison. The DRR and look-up EPID images were shown in Figure 24.

Figure 25 shows summed gamma values by comparing the DRR with each phase of look-up EPID image. The result shows that the minimum gamma value was found at the phase 3, which is matching to the phase of DRR. Figure 26 shows actual 2D gamma distribution where the DRR was compared with look-up EPID image of phase 3 and 5. In Figure 26 (a), there was high gamma value region at the dose gradient region; it was considered that the pixel response in DRR was different from that of EPID image. When gamma values were calculated with the look-up image at phase 5, similar discrepancy was observed, where additional mismatch appeared around the tumor. The phase of "measured" EPID image was successfully determined as phase 3.

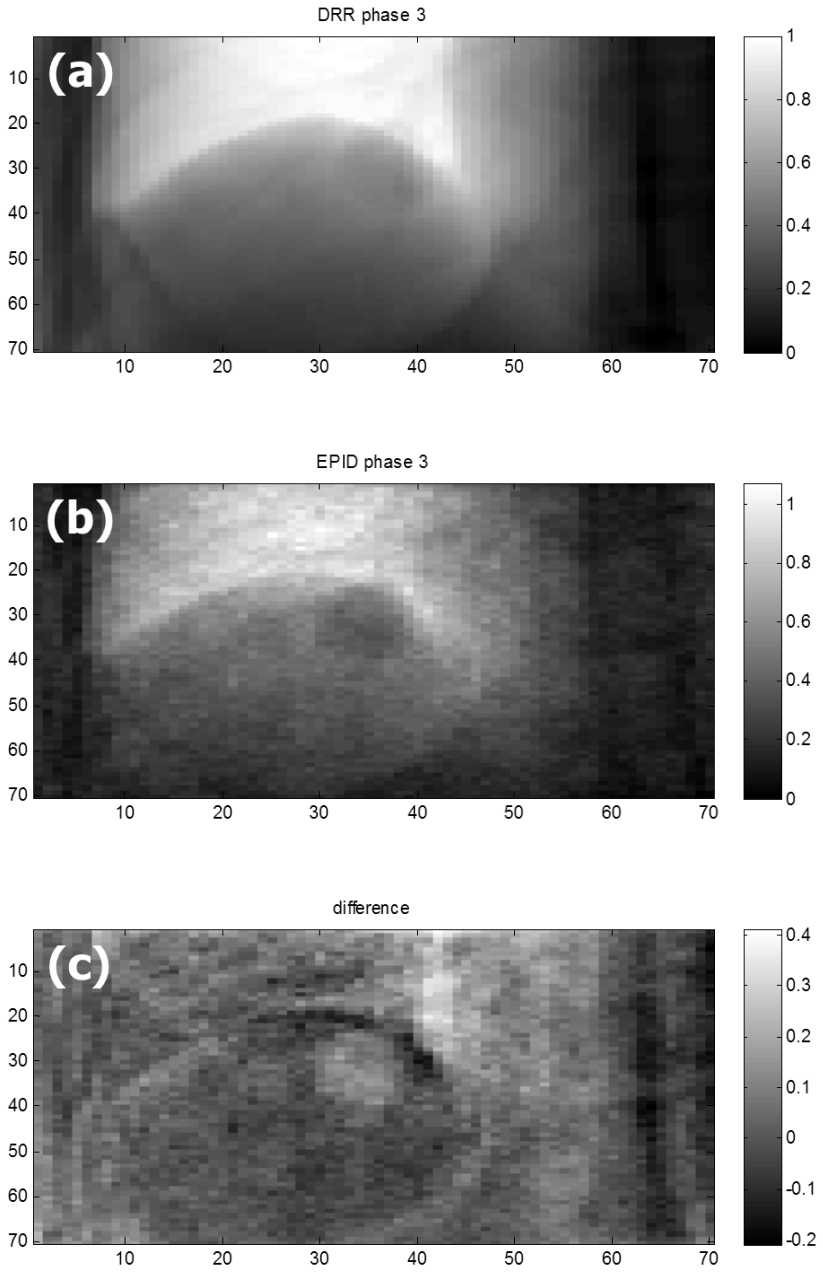

Figure 24. MV images used for the phase sorting evaluation. The images were calculated from digital XCAT phantom. (a) Generated DRR image and (b) look-up EPID image for phase 3. The difference between (a) and (b) is shown in (c). The pixel resolution was 3.1 x 1.6 mm^2.

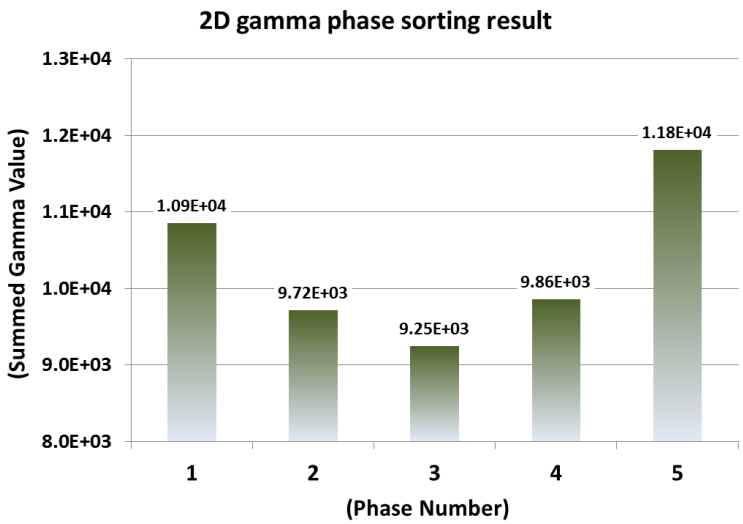

Figure 25. Summed gamma values by comparing the DRR (regarded as a measured EPID image) with look-up EPID images simulated from digital XCAT phantom.

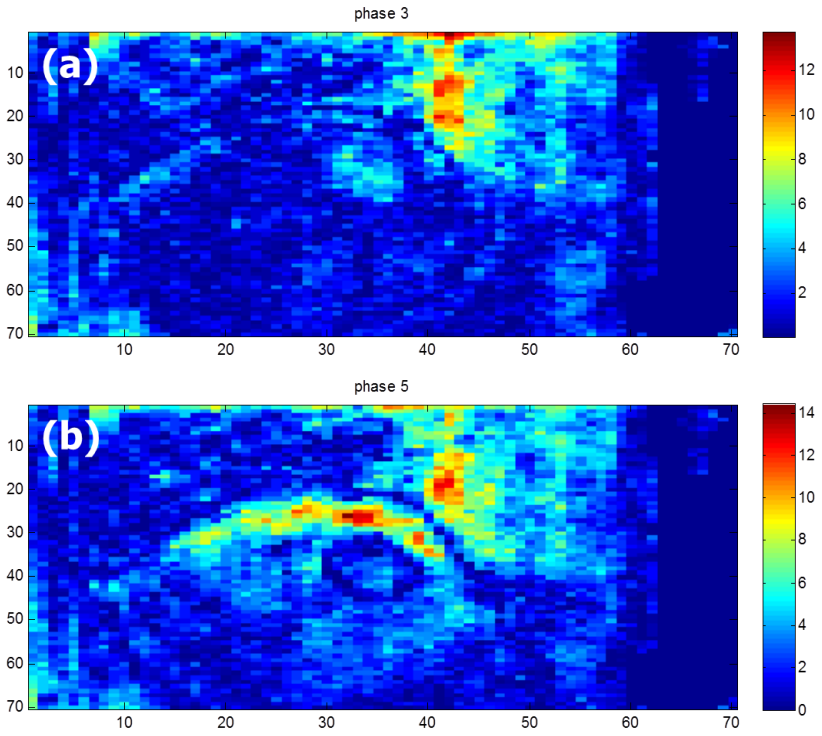

Figure 26. 2D gamma evaluation map for the phase sorting. The "measured" EPID image in phase 3 was compared with look-up EPID image at (a) phase 3 and (b) phase 5, respectively

4. CONCLUSION

4.1EPID modeling in XVMC codes

A new model of EPID in the XVMC code was developed by incorporating effective atomic numbers of elemental components of EPID structures and adopting the phase space source from the EGSnrc code into the density-scaled model previously developed [71]. A virtual detector model [58] of EPID was also developed in the EGSnrc code. The EGSnrc and XVMC codes in water phantom at the plane of EPID were found to perform within the accuracy of 3.9 and 2.8%, respectively. For the EPID image comparison, using the calibration factors that are dependent on field sizes and thicknesses for the conversion of calculated images to measured images, the EGSnrc and XVMC models were found to perform within the accuracies of 1.4 and 1.9%, respectively. Since the raw pixel value on the measured EPID image is not an absolute value that can be physically interpreted but requires additional calibration depends on measurement condition, the values were normalized at 10×10 cm^2 field size under a 20 cm homogeneous phantom in this study. As a result, the differences in the EPID simulations were lower than that of water dose comparison.

The Z_{eff} correction incorporated into the XVMC model improved physical performance of the calibration factors, compared with that of the density-only-scaled model. The use of phase space files from the EGSnrc/BEAMnrc code significantly improved agreement of calculated profiles with measured profiles in penumbra regions. Demonstrating superior accuracy, the two MC models may be used for accurate *in vivo* dosimetry of radiation therapy. However, significant amounts of calculation time can be saved by using the XVMC model (12.4 times

faster). Therefore, the EPID image prediction model in XVMC code was used in the 4D dose reconstruction with phase sorting method and further evaluated.

4.2Four-dimensional dose reconstruction with the phase sorting method

A 4D dose reconstruction method with phase-sorted cine EPID images for a breathing phantom was developed and demonstrated. The acquired cine EPID images during a treatment were determined by comparing with predicted look-up EPID images and assigned to the reference phases by 2D gamma method. For the phases that the tumor was shadowed by the MLCs, the phase was determined manually by breathing phase extrapolation from the known breathing motion. The dose was reconstructed based on the measured EPID images by non-iterative inverse method and compared with forward calculations on 4D CT, MIP and AIP. The reconstructed doses were evaluated by 2D gamma and DVH analysis. The reconstructed doses showed good agreements with the forward 4D dose calculations, where showed difference from the static 3D dose calculation on MIP or AIP. The difference in DVH was expected since the tumor volume to PTV ratio was not the same in 3D and 4D planning.

The phase determination was performed by 2D gamma method in this study and the results were good for the cases studied. Other methods may be used for the phase sorting, such as center of mass method (comparing the location of the center of the tumor on the EPID image) or 2D image deformation technique. However, the differences among possible candidates were not evaluated in this study; another phase sorting method could be better for complex anatomy or extreme case. The effect from using another phase sorting method may be evaluated in the future.

The suggested 2D gamma method was also evaluated with an anthropomorphic deformable digital XCAT phantom. Since an EPID image cannot be obtained from digital phantom, an MV DRR image was generated for an arbitrary phase and regarded as a measured EPID image in this study. The summed gamma value was lowest at the phantom phase where the DRR was generated. Therefore, the 2D gamma method for the phase sorting yielded an accurate result for the deformable anthropomorphic phantom simulation.

The accuracy of the reconstructed dose is determined by the accuracy of the CT image and the predicted EPID image. In this experiment, the same CT images were used for the planning (forward dose calculation) and the *in vivo* dosimetry (dose reconstruction). Therefore, in this study, the agreement between forward calculation and reconstruction is determined by the accuracy of the EPID image prediction as well as the accuracy of phase sorting method. It can be concluded, therefore, the good agreement of 2D gamma and DVH comparison between 4D forward calculation and reconstruction implies that the EPID simulation model was able to predict accurate EPID images in this study.

5. FUTURE WORKS

5.1Future work : 4D CT extension method

The fast and accurate EPID image prediction model and the 4D dose reconstruction method for *in vivo* dosimetry were developed. As described above, however, the accuracy is limited by the accuracy of the CT image and the predicted EPID image. The latter was improved by the new EPID model suggested in this study. However, tumor position or patient geometry during treatment is still unknown and unpredictable, especially when the patients' breathing is not reproducible between CT acquisition and treatment. Moreover, if the patient breathing motion is bigger than expected, the current phase sorting method would not provide an accurate reconstructed dose to the patient, since the 4D CT image corresponding to the abnormal breathing phase does not exist. When the breathing motion extent exceeded from that presented by plan CTs, the problem will be solved if the corresponding patient CT image of the phase is presented. Since the breathing phase of this unexpected motion was not obtained from the 4D CT, a new CT image should be generated by reconstruction from the pre-acquired CT images.

To represent the patient at the time of treatment, a CT reconstruction method was tested when the respiratory motion of a patient deviated from a motion range that is representative of the initial CT [109]. The method utilizes a motion vector acquired from a plan CT and motion extent visible in cine EPID images. A feasibility study was performed for the 4D CT extension as following.

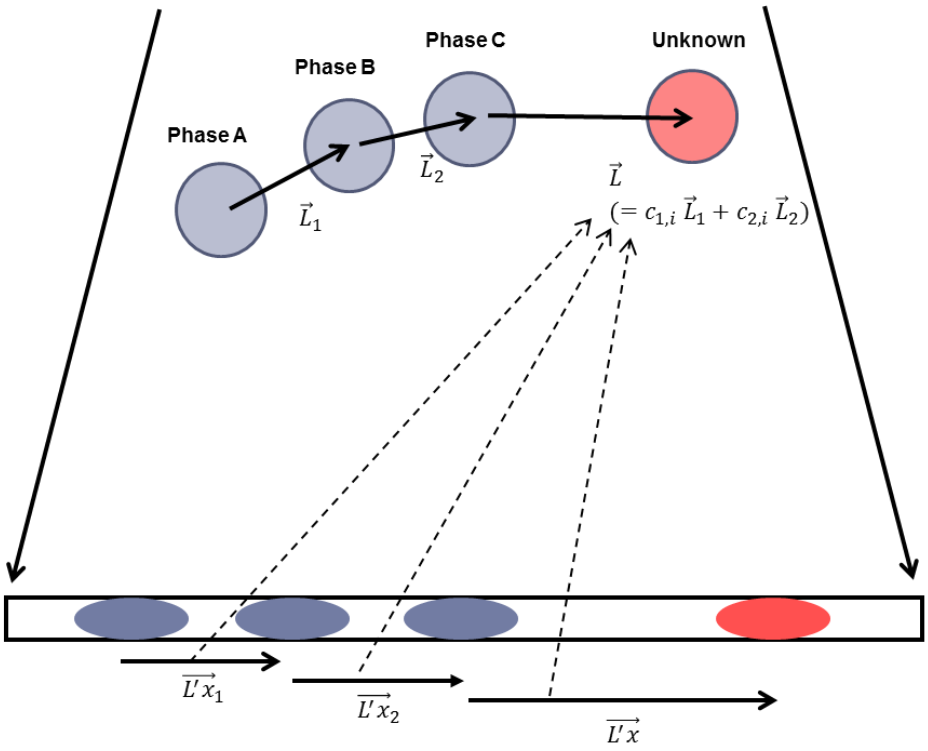

Figure 27. Schematic diagram of deform vector correlation with tumor location on portal images. The acquired EPID image is deviated (red circle) where the motion was greater than expected amplitude (blue circle) within fixed jaw opening. The motion vectors between phases were weighted by the displacement of tumor location on 2D portal images.

To generate a new 4D CT image of the treatment day from the old 4D CT and the portal images of the day when the motion extent exceeded from that represented by plan CTs, a motion vector of a moving tumor in a patient may be extended to reconstruct the tumor position when the motion extent exceeded the plan CTs. To test this, a phantom that consists of a polystyrene cylinder (tumor) embedded in cork (lung) was placed on a moving platform with 4 sec/cycle and amplitudes of 1 cm and 2 cm, and was 4D-scanned. Then, a 6MV photon beam was irradiated on the moving phantoms and cine EPID images were obtained. On cine EPID images of the 1 cm

case, the tumor was outlined and marked for the displacement vector calculation (see blue tumors in Figure 27). The displacement vector was calculated based on the correlation of CT and EPID images of each phase. When the motion extent exceeded the initial extent (1 cm), the displacement on EPID was obtained through tumor outlining and calculation of center-of-mass travel (Figure 28), and programmed into the calculated displacement vector. A new CT image was thus reconstructed, and compared with the pre-acquired actual CT image (Figure 29). They showed a slight mismatch in the transition direction limited by voxel size (slice thickness) in CT image. Due to the rigid nature of the studied phantom, the modeling the displacement of the center of object was sufficient. When deformable tumors are to be modeled, more complex scheme is necessary, which utilize cine EPID and 4D CT images.

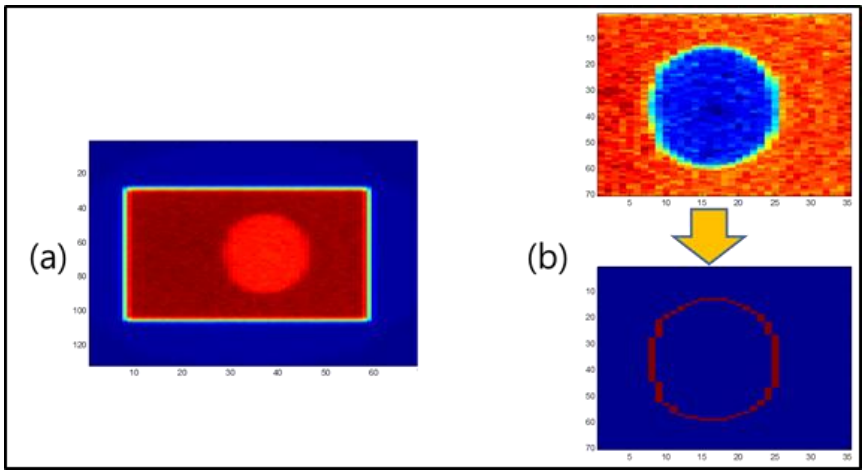

Figure 28. Edge detection method was shown. (a) In EPID image, a tumor to be outlined was shown. (b) To find out the center of mass, the edge was detected on in-field region of EPID image and corresponding voxel transition vector was determined within 4D CTs.

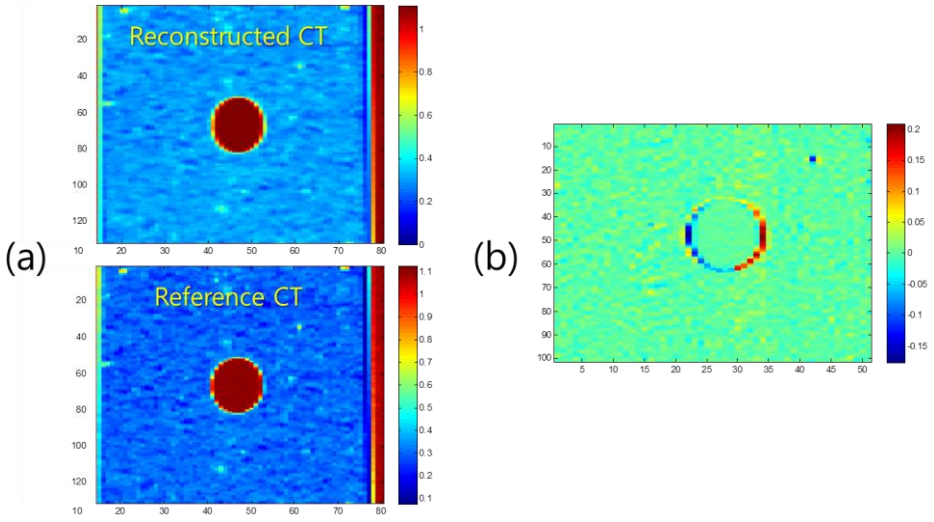

Figure 29. Cross-sectional view at the isocenter plane. (a) Reference CT image of 2cm amplitude motion with 50% phase (upper), and reconstructed CT image for the same condition by the vector extension method (lower). The reference CT image was obtained from 4D CTs with the given condition, for the comparison purpose. (b) Density difference map between reference and reconstructed CTs was shown around the tumor. Slight mismatch in x-direction is mainly due to the limitation of the resolution in CT slice (2.5 mm)

As the CT reconstruction method was successful for the rigid phantom, the method was further evaluated using an anthropomorphic XCAT phantom. Phantom geometries according to breathing motion were digitally generated; the generated phantoms were regarded as CT images in this evaluation. The diaphragm motion was 2 cm amplitude with 4 sec period. A spherical shaped tumor was placed in the lower lobe of the lung with 2 cm diameter, where the location was changed by the organ deformation according to the breathing motion, as shown in Figure 30. The breathing motion was separated in 10 phases, where phase 1 was maximum exhale and

phase 6 was maximum inhale. For the test, it was assumed that CT images for phase 1~5 only were known, where phase 6 was regarded as “unknown” and used for evaluation purpose only.

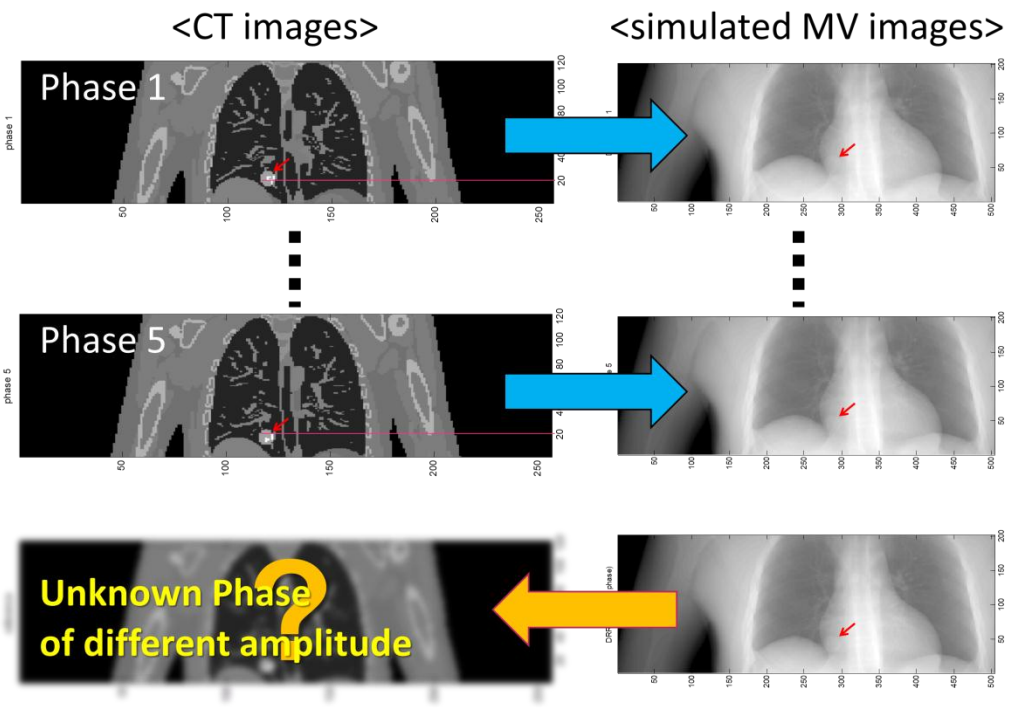

Figure 30. CT images and corresponding MV images for the evaluation of CT extension. (Blue Arrows); CT images for phase 1~5 and corresponding MV images were generated using XCAT phantom. (Orange Arrow); The aim of this method is to reconstruct CT image of unknown phase using acquired portal image, where the tumor location is exceeded from the expectation.

Since the linear transition model suggested in the rigid phantom case cannot be used in the deformable anthropomorphic phantom, the CT image of “unknown” phase was reconstructed by following steps. (1) Deformation vectors between phases were obtained. (2) Also, tumor

locations were found from the simulated MV images. (3) Finally, the deformation vectors were linearly weighted by the displacement of the tumor location (i.e., center of mass) on EPID images and a new CT image was reconstructed.

Figure 31 shows cross-sectional images of the (a)“reconstructed” and (b)”ground truth” CTs. The reconstructed image was blurred, compared with the “ground truth” CT image. They were inter-compared by (c)cross-sectional profiles and (d)differences in HU values. The reconstructed profile showed blurring at the edge of the tumor and other organs. The reconstructed tumor location was accurate in displacement less than 3 mm, where it was less than 1.6 mm for the most points. The difference in HU (Figure 31-d) was mainly due to image blurring of the reconstructed CT.

As a result, the suggested method was able to reconstruct the CT image of “unknown” phase based on an acquired portal image. Clinical acceptability of the suggested method will further verified by DVH study.

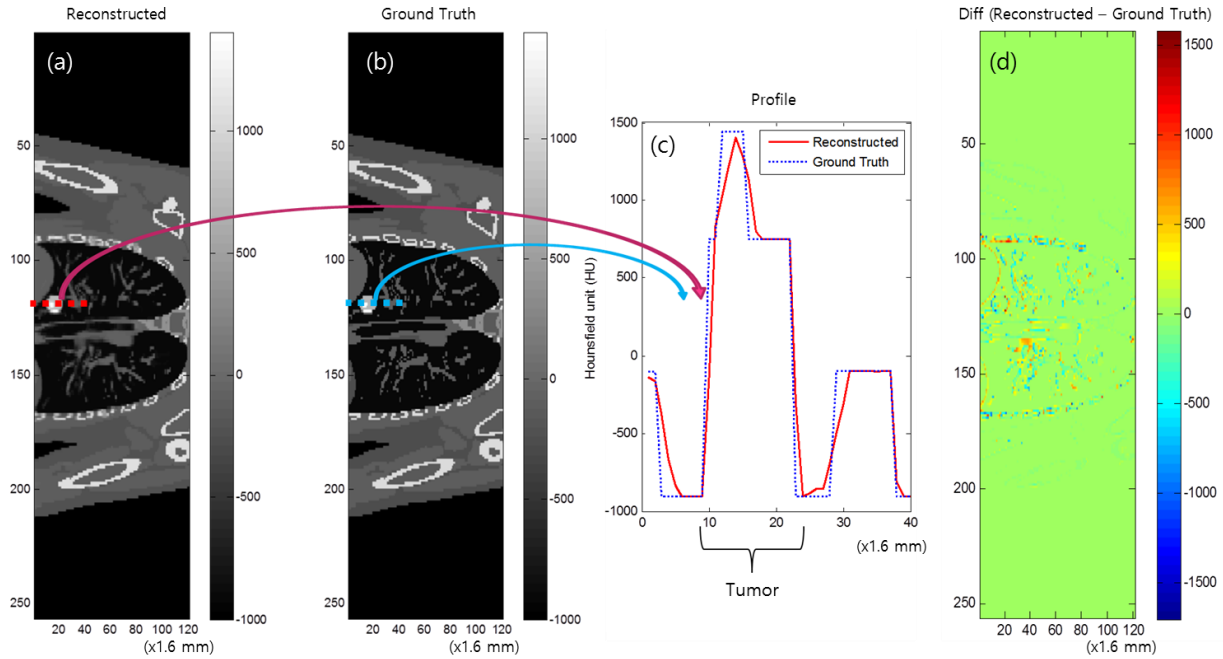

Figure 31. 4D CT extension result for the anthropomorphic digital phantom. CT images for (a) reconstructed and (b) ground truth were shown. The resolution was 1.6x3.1 mm^2. (c) Profiles near the tumor (on the red dotted line) were shown in (c). The x-axis resolution was 1.6 mm and the displacement of the tumor location was less than 1.6 mm. Difference between (a) and (b) in HU was shown in (d).

5.2Future work : alternative method for 4D CT reconstruction

When the tumor position was shifted in lateral (parallel to the EPID plane) direction, it will be shown on the EPID image and therefore can be detected in the phase sorting step. However, for z-direction (perpendicular to the EPID plane) shift, it cannot be seen on the EPID image unless gantry angle was changed. If the tumor location shift (mostly baseline shift in this

case) appears in certain gantry angle, it may imply that the position of the tumor was changed. In this case, suggested 4D CT reconstruction method cannot be used.

The method using EPID images to reconstruct patient anatomy has been studied [79], [80]. However, the direct MV-CT reconstruction method is limited when there is not enough angular information provided. Also, the reconstructed density is not as accurate as kV-CT.

An alternative method to obtain an accurate CT image could be using a partial reconstruction, based on kV-CT by comparing measured EPID images with predictions. From the dose reconstruction equation,

$$E = R_E\, I \quad \rightarrow \quad R_E = \int K_E\, e^{-\mu x}\, dV \tag{6}$$

$$E^c = R_E^c\, I^c \quad \rightarrow \quad R_E^c = \int K_E^c\, e^{-\mu_c x}\, dV \tag{7}$$

then, combining Eq. (6) and (7), it can be found that

$$\frac{E_c}{E} = \frac{R_E^c I^c}{R_E I} = \frac{\int K_E^c\, I\, e^{-\mu_c x}\, dV}{\int K_E\, I\, e^{-\mu x}\, dV} \cong e^{-(\mu_c - \mu)x} = \sum_n exp(-(\mu_{c,n} - \mu_n)x) \tag{8}$$

assuming the beam hardening and scattering did not change at the EPID.

From Eq. (8), the change in attenuation coefficients in a voxel can be found from the change in EPID image responses. The change in attenuation coefficients is then converted in density change in each voxel of original CT images. Finally, the CT image can be reconstructed using pre-obtained kV-CT image by change density values of each voxel. This method may be used in multiple-gantry IMRT or VMAT to reconstruct CT image.

REFERENCES

[1] G. a. Ezzell, J. M. Galvin, D. Low, J. R. Palta, I. Rosen, M. B. Sharpe, P. Xia, Y. Xiao, L. Xing, and C. X. Yu, "Guidance document on delivery, treatment planning, and clinical implementation of IMRT: Report of the IMRT subcommittee of the AAPM radiation therapy committee," *Med. Phys.*, vol. 30, no. 8, p. 2089, 2003.

[2] J. R. Palta, C. Liu, and J. G. Li, "Current External Beam Radiation Therapy Quality Assurance Guidance: Does It Meet the Challenges of Emerging Image-Guided Technologies?," *Int. J. Radiat. Oncol. Biol. Phys.*, vol. 71, no. 1 SUPPL., pp. 13–17, 2008.

[3] G. a. Ezzell, J. W. Burmeister, N. Dogan, T. J. LoSasso, J. G. Mechalakos, D. Mihailidis, A. Molineu, J. R. Palta, C. R. Ramsey, B. J. Salter, J. Shi, P. Xia, N. J. Yue, and Y. Xiao, "IMRT commissioning: Multiple institution planning and dosimetry comparisons, a report from AAPM Task Group 119," *Med. Phys.*, vol. 36, no. 11, p. 5359, 2009.

[4] J. M. Kapatoes, G. H. Olivera, K. J. Ruchala, J. B. Smilowitz, P. J. Reckwerdt, and T. R. Mackie, "A feasible method for clinical delivery verification and dose reconstruction in tomotherapy.," *Med. Phys.*, vol. 28, no. 4, pp. 528–42, Apr. 2001.

[5] L. N. McDermott, M. Wendling, J. Nijkamp, A. Mans, J.-J. Sonke, B. J. Mijnheer, and M. van Herk, "3D in vivo dose verification of entire hypo-fractionated IMRT treatments using an EPID and cone-beam CT," *Radiother. Oncol.*, vol. 86, no. 1, pp. 35–42, Jan. 2008.

[6] W. van Elmpt, S. Nijsten, S. Petit, B. Mijnheer, P. Lambin, and A. Dekker, "3D in vivo dosimetry using megavoltage cone-beam CT and EPID dosimetry," *Int. J. Radiat. Oncol. Biol. Phys.*, vol. 73, no. 5, pp. 1580–7, Apr. 2009.

[7] B. Mijnheer, S. Beddar, J. Izewska, and C. Reft, "In vivo dosimetry in external beam radiotherapy," *Med. Phys.*, vol. 40, no. 7, p. 070903, Jul. 2013.

[8] A. Piermattei, A. Fidanzio, G. Stimato, L. Azario, L. Grimaldi, G. D'Onofrio, S. Cilla, M. Balducci, M. A. Gambacorta, N. Di Napoli, and N. Cellini, "In vivo dosimetry by an aSi-based EPID," *Med. Phys.*, vol. 33, no. 11, p. 4414, 2006.

[9] L. Ren, Y. Zhang, and F.-F. Yin, "A limited-angle intrafraction verification (LIVE) system for radiation therapy.," *Med. Phys.*, vol. 41, no. 2, p. 020701, Feb. 2014.

[10] W. van Elmpt, G. a Ezzell, and C. G. Orton, "Point/Counterpoint. EPID dosimetry must soon become an essential component of IMRT quality assurance.," *Med. Phys.*, vol. 36, no. 10, pp. 4325–4327, 2009.

[11] T. Fuangrod, H. C. Woodruff, E. van Uytven, B. M. C. McCurdy, Z. Kuncic, D. J. O'Connor, and P. B. Greer, "A system for EPID-based real-time treatment delivery verification during dynamic IMRT treatment," *Med. Phys.*, vol. 40, no. 9, p. 091907, 2013.

[12] D. a Low, W. B. Harms, S. Mutic, and J. a Purdy, “A technique for the quantitative evaluation of dose distributions.,” *Med. Phys.*, vol. 25, no. 5, pp. 656–61, May 1998.

[13] T. Ju, T. Simpson, J. O. Deasy, and D. a. Low, “Geometric interpretation of the gamma dose distribution comparison technique: interpolation-free calculation.,” *Med. Phys.*, vol. 35, no. 3, pp. 879–87, Mar. 2008.

[14] B. E. Nelms, H. Zhen, and W. A. Tomé, “Per-beam, planar IMRT QA passing rates do not predict clinically relevant patient dose errors.,” *Med. Phys.*, vol. 38, no. 2, pp. 1037–44, Feb. 2011.

[15] K. Tanderup, S. Beddar, C. E. Andersen, G. Kertzscher, and J. E. Cygler, “In vivo dosimetry in brachytherapy.,” *Med. Phys.*, vol. 40, no. 7, p. 070902, Jul. 2013.

[16] J. L. Leman, “In vivo dosimetry; essential or unnecessary?,” *J. Radiother. Pract.*, vol. 11, no. 01, pp. 55–61, Apr. 2011.

[17] N. Tyagi, K. Yang, D. Gersten, and D. Yan, “A real time dose monitoring and dose reconstruction tool for patient specific VMAT QA and delivery.,” *Med. Phys.*, vol. 39, no. 12, pp. 7194–204, Dec. 2012.

[18] M.-H. Lin, J. Li, L. Wang, S. Koren, J. Fan, E. Forkal, and C.-M. Ma, “4D patient dose reconstruction using online measured EPID cine images for lung SBRT treatment validation.,” *Med. Phys.*, vol. 39, no. 10, pp. 5949–58, Oct. 2012.

[19] I. J. Yeo, J. W. Jung, B. Y. Yi, and J. O. Kim, “Feasibility study on inverse four-dimensional dose reconstruction using the continuous dose-image of EPID,” *Med. Phys.*, vol. 40, no. 5, p. 051702, 2013.

[20] D. Opp, B. E. Nelms, G. Zhang, C. Stevens, and V. Feygelman, “Validation of measurement-guided 3D VMAT dose reconstruction on a heterogeneous anthropomorphic phantom.,” *J. Appl. Clin. Med. Phys.*, vol. 14, no. 4, p. 4154, Jan. 2013.

[21] B. E. Nelms, M. F. Chan, G. Jarry, M. Lemire, J. Lowden, C. Hampton, and V. Feygelman, “Evaluating IMRT and VMAT dose accuracy: Practical examples of failure to detect systematic errors when applying a commonly used metric and action levels.,” *Med. Phys.*, vol. 40, no. 11, p. 111722, Nov. 2013.

[22] B. E. Nelms, D. Opp, J. Robinson, T. K. Wolf, G. Zhang, E. Moros, and V. Feygelman, “VMAT QA: measurement-guided 4D dose reconstruction on a patient.,” *Med. Phys.*, vol. 39, no. 7, pp. 4228–38, Jul. 2012.

[23] E. Schreibmann, A. Dhabaan, E. Elder, and T. Fox, “Patient-specific quality assurance method for VMAT treatment delivery.,” *Med. Phys.*, vol. 36, no. 10, pp. 4530–5, Oct. 2009.

[24] H. C. Woodruff, T. Fuangrod, P. Rowshanfarzad, B. M. C. McCurdy, and P. B. Greer, "Gantry-angle resolved VMAT pretreatment verification using EPID image prediction.," *Med. Phys.*, vol. 40, no. 8, p. 081715, Aug. 2013.

[25] a Manikandan, B. Sarkar, R. Holla, T. R. Vivek, and N. Sujatha, "Quality assurance of dynamic parameters in volumetric modulated arc therapy.," *Br. J. Radiol.*, vol. 85, no. 1015, pp. 1002–10, Jul. 2012.

[26] J. Rottmann, P. Keall, and R. Berbeco, "Markerless EPID image guided dynamic multi-leaf collimator tracking for lung tumors.," *Phys. Med. Biol.*, vol. 58, no. 12, pp. 4195–204, Jun. 2013.

[27] T. R. McNutt, T. R. Mackie, P. Reckwerdt, and B. R. Paliwal, "Modeling dose distributions from portal dose images using the convolution/superposition method.," *Medical physics*, vol. 23, no. 8. pp. 1381–92, Aug-1996.

[28] R. J. W. Louwe, E. M. F. Damen, M. van Herk, a. W. H. Minken, O. Törzsök, and B. J. Mijnheer, "Three-dimensional dose reconstruction of breast cancer treatment using portal imaging.," *Med. Phys.*, vol. 30, no. 9, pp. 2376–89, Sep. 2003.

[29] S. C. Vieira, M. L. P. Dirkx, B. J. M. Heijmen, and H. C. J. de Boer, "SIFT: a method to verify the IMRT fluence delivered during patient treatment using an electronic portal imaging device.," *Int. J. Radiat. Oncol. Biol. Phys.*, vol. 60, no. 3, pp. 981–93, Nov. 2004.

[30] A. L. Fielding, P. M. Evans, and C. H. Clark, "Verification of patient position and delivery of IMRT by electronic portal imaging.," *Radiother. Oncol.*, vol. 73, no. 3, pp. 339–47, Dec. 2004.

[31] M. Wendling, R. J. W. Louwe, L. N. McDermott, J.-J. Sonke, M. van Herk, and B. J. Mijnheer, "Accurate two-dimensional IMRT verification using a back-projection EPID dosimetry method.," *Med. Phys.*, vol. 33, no. 2, pp. 259–73, Feb. 2006.

[32] M. Partridge, M. Ebert, and B. M. Hesse, "IMRT verification by three-dimensional dose reconstruction from portal beam measurements.," *Med. Phys.*, vol. 29, no. 8, pp. 1847–58, Aug. 2002.

[33] V. N. Hansen, P. M. Evans, and W. Swindell, "The application of transit dosimetry to precision radiotherapy.," *Med. Phys.*, vol. 23, no. 5, pp. 713–21, May 1996.

[34] G. Jarry and F. Verhaegen, "Patient-specific dosimetry of conventional and intensity modulated radiation therapy using a novel full Monte Carlo phase space reconstruction method from electronic portal images.," *Phys. Med. Biol.*, vol. 52, no. 8, pp. 2277–99, Apr. 2007.

[35] I. J. Yeo, J. W. Jung, M. Chew, J. O. Kim, B. Wang, S. Dibiase, Y. Zhu, and D. Lee, "Dose reconstruction for intensity-modulated radiation therapy using a non-iterative method and portal dose image.," *Phys. Med. Biol.*, vol. 54, no. 17, pp. 5223–36, Sep. 2009.

[36] G. V. Menon and R. S. Sloboda, "Quality assurance measurements of a-Si EPID performance," *Med. Dosim.*, vol. 29, no. 1, pp. 11–17, 2004.

[37] L. E. Antonuk, "Electronic portal imaging devices: a review and historical perspective of contemporary technologies and research.," *Phys. Med. Biol.*, vol. 47, no. 6, pp. R31–R65, 2002.

[38] "Tutorial on EPID." [Online]. Available: http://radonc.ucsf.edu/research_group/jpouliot/tutorial/HU/Lesson2.htm.

[39] B. E. Nelms, K. H. Rasmussen, and W. A. Tome, "Evaluation of a fast method of EPID-based dosimetry for intensity-modulated radiation therapy.," *J. Appl. Clin. Med. Phys.*, vol. 11, no. 2, p. 3185, Jan. 2010.

[40] P. B. Greer and C. C. Popescu, "Dosimetric properties of an amorphous silicon electronic portal imaging device for verification of dynamic intensity modulated radiation therapy," *Med. Phys.*, vol. 30, no. 7, p. 1618, 2003.

[41] C. Kirkby and R. Sloboda, "Consequences of the spectral response of an a-Si EPID and implications for dosimetric calibration.," *Med. Phys.*, vol. 32, no. 8, pp. 2649–2658, 2005.

[42] Y. El-Mohri, L. E. Antonuk, J. Yorkston, K. W. Jee, M. Maolinbay, K. L. Lam, and J. H. Siewerdsen, "Relative dosimetry using active matrix flat-panel imager (AMFPI) technology.," *Med. Phys.*, vol. 26, no. 8, pp. 1530–1541, 1999.

[43] J. Yoon, J. Kim, J. Jung, and I. Yeo, "Exit EPID Image Prediction Below Heterogeneous Phantoms Using Monte Carlo Codes," *Med. Phys.*, vol. 40, no. 6, p. 240, 2013.

[44] H. C. Woodruff and P. B. Greer, "3D Dose reconstruction: Banding artefacts in cine mode EPID images during VMAT delivery," *J. Phys. Conf. Ser.*, vol. 444, p. 012042, Jun. 2013.

[45] I. J. Yeo, J. W. Jung, B. Patyal, A. Mandapaka, B. Y. Yi, and J. O. Kim, "Conditions for reliable time-resolved dosimetry of electronic portal imaging devices for fixed-gantry IMRT and VMAT.," *Med. Phys.*, vol. 40, no. 7, p. 072102, Jul. 2013.

[46] A. Van Esch, T. Depuydt, and D. P. Huyskens, "The use of an aSi-based EPID for routine absolute dosimetric pre-treatment verification of dynamic IMRT fields.," *Radiother. Oncol.*, vol. 71, no. 2, pp. 223–34, May 2004.

[47] T. R. McNutt, T. R. Mackie, P. Reckwerdt, N. Papanikolaou, and B. R. Paliwal, "Calculation of portal dose using the convolution/superposition method," *Med. Phys.*, vol. 23, no. 4, pp. 527–35, Apr. 1996.

[48] V. N. Hansen, W. Swindell, and P. M. Evans, "Extraction of primary signal from EPIDs using only forward convolution," *Med. Phys.*, vol. 24, no. 9, pp. 1477–84, Sep. 1997.

[49] K. L. Pasma, B. J. Heijmen, M. Kroonwijk, and a G. Visser, "Portal dose image (PDI) prediction for dosimetric treatment verification in radiotherapy. I. An algorithm for open beams," *Med. Phys.*, vol. 25, no. 6, pp. 830–40, Jun. 1998.

[50] B. M. McCurdy and S. Pistorius, "A two-step algorithm for predicting portal dose images in arbitrary detectors," *Med. Phys.*, vol. 27, no. 9, pp. 2109–16, Sep. 2000.

[51] L. Spies and T. Bortfeld, "Analytical scatter kernels for portal imaging at 6 MV," *Med. Phys.*, vol. 28, no. 4, pp. 553–9, Apr. 2001.

[52] C. V. Dahlgren, A. Ahnesjö, A. Montelius, and G. Rikner, "Portal dose image verification: formalism and application of the collapsed cone superposition method," *Phys. Med. Biol.*, vol. 47, no. 24, pp. 4371–87, Dec. 2002.

[53] W. J. C. van Elmpt, S. M. J. J. G. Nijsten, B. J. Mijnheer, and a. W. H. Minken, "Experimental verification of a portal dose prediction model," *Med. Phys.*, vol. 32, no. 9, pp. 2805–18, Sep. 2005.

[54] W. van Elmpt, L. McDermott, S. Nijsten, M. Wendling, P. Lambin, and B. Mijnheer, "A literature review of electronic portal imaging for radiotherapy dosimetry," *Radiother. Oncol.*, vol. 88, no. 3, pp. 289–309, Sep. 2008.

[55] B. M. McCurdy, K. Luchka, and S. Pistorius, "Dosimetric investigation and portal dose image prediction using an amorphous silicon electronic portal imaging device," *Med. Phys.*, vol. 28, no. 6, pp. 911–24, Jun. 2001.

[56] B. Warkentin, S. Steciw, S. Rathee, and B. G. Fallone, "Dosimetric IMRT verification with a flat-panel EPID," *Med. Phys.*, vol. 30, no. 12, pp. 3143–55, Dec. 2003.

[57] K. Chytyk and B. M. C. McCurdy, "Investigation of tilted dose kernels for portal dose prediction in a-Si electronic portal imagers," *Med. Phys.*, vol. 33, no. 9, pp. 3333–9, Sep. 2006.

[58] J. V. Siebers, J. O. Kim, L. Ko, P. J. Keall, and R. Mohan, "Monte Carlo computation of dosimetric amorphous silicon electronic portal images," *Med. Phys.*, vol. 31, no. 7, pp. 2135–46, Jul. 2004.

[59] L. Parent, J. Seco, P. M. Evans, A. Fielding, and D. R. Dance, "Monte Carlo modelling of a-Si EPID response: the effect of spectral variations with field size and position," *Med. Phys.*, vol. 33, no. 12, pp. 4527–40, Dec. 2006.

[60] E. Spezi and D. G. Lewis, "Full forward Monte Carlo calculation of portal dose from MLC collimated treatment beams," *Phys. Med. Biol.*, vol. 47, no. 3, pp. 377–90, Feb. 2002.

[61] I. Fotina, P. Winkler, T. Künzler, J. Reiterer, I. Simmat, and D. Georg, "Advanced kernel methods vs. Monte Carlo-based dose calculation for high energy photon beams.," *Radiother. Oncol.*, vol. 93, no. 3, pp. 645–53, Dec. 2009.

[62] W. R. Nelson, H. Hirayamal, and D. W. Rogersfbl, "THE EGS4 CODE SYSTEM," 1985.

[63] E. Vanetti De' Palma, L. Conte, G. Nicolini, P. Stucchi, C. Mordacchini, E. Cassani, and R. Novario, "Experimental method to obtain scattering contribution in portal dose images," *Phys. Med.*, vol. 21, no. 1, pp. 31–40, 2005.

[64] P. Rowshanfarzad, M. Sabet, D. J. O'Connor, and P. B. Greer, "Impact of backscattered radiation from the bunker structure on EPID dosimetry," *J. Appl. Clin. Med. Phys.*, vol. 13, no. 6, p. 4024, Jan. 2012.

[65] B. A. Faddegon, I. Kawrakow, Y. Kubyshin, J. Perl, J. Sempau, and L. Urban, "The accuracy of EGSnrc, Geant4 and PENELOPE Monte Carlo systems for the simulation of electron scatter in external beam radiotherapy.," *Phys. Med. Biol.*, vol. 54, no. 20, pp. 6151–63, Oct. 2009.

[66] "EGSnrc: software tool to model radiation transport - National Research Council Canada," May 2013.

[67] P. Vaz, "Monte Carlo methods and techniques status and prospects for future evolution.," *Appl. Radiat. Isot.*, vol. 68, no. 4–5, pp. 536–41, 2010.

[68] I. J. Chetty, B. Curran, J. E. Cygler, J. J. DeMarco, G. Ezzell, B. a. Faddegon, I. Kawrakow, P. J. Keall, H. Liu, C.-M. C. Ma, D. W. O. Rogers, J. Seuntjens, D. Sheikh-Bagheri, and J. V. Siebers, "Report of the AAPM Task Group No. 105: Issues associated with clinical implementation of Monte Carlo-based photon and electron external beam treatment planning," *Med. Phys.*, vol. 34, no. 12, p. 4818, 2007.

[69] K. Babcock, G. Cranmer-Sargison, and N. Sidhu, "Increasing the speed of DOSXYZnrc Monte Carlo simulations through the introduction of nonvoxelated geometries.," *Med. Phys.*, vol. 35, no. 2, pp. 633–44, Feb. 2008.

[70] J. Lippuner and I. a Elbakri, "A GPU implementation of EGSnrc's Monte Carlo photon transport for imaging applications.," *Phys. Med. Biol.*, vol. 56, no. 22, pp. 7145–62, Nov. 2011.

[71] J. W. Jung, J. O. Kim, I. J. Yeo, Y.-B. Cho, S. M. Kim, and S. Dibiase, "Fast transit portal dosimetry using density-scaled layer modeling of aSi-based electronic portal imaging device and Monte Carlo method," *Med. Phys.*, vol. 39, no. 12, pp. 7593–602, Dec. 2012.

[72] M. Fippel, "Fast Monte Carlo dose calculation for photon beams based on the VMC electron algorithm," *Med. Phys.*, vol. 26, no. 8, pp. 1466–75, Aug. 1999.

[73] I. Kawrakow and M. Fippel, "Investigation of variance reduction techniques for Monte Carlo photon dose calculation using XVMC.," *Phys. Med. Biol.*, vol. 45, pp. 2163–2183, 2000.

[74] I. Kawrakow and D. W. O. Rogers, "The EGSnrc code system: Monte Carlo simulation of electron and photon transport," *Ioniz. Radiat. Stand. Natl. Res. Counc. Canada Tech. Rep. No. PIRS-701*, 2003.

[75] C.-S. Chui, E. Yorke, and L. Hong, "The effects of intra-fraction organ motion on the delivery of intensity-modulated field with a multileaf collimator," *Med. Phys.*, vol. 30, no. 7, p. 1736, 2003.

[76] Y. Seppenwoolde, H. Shirato, K. Kitamura, S. Shimizu, M. van Herk, J. V Lebesque, and K. Miyasaka, "Precise and real-time measurement of 3D tumor motion in lung due to breathing and heartbeat, measured during radiotherapy.," *Int. J. Radiat. Oncol. Biol. Phys.*, vol. 53, no. 4, pp. 822–34, Jul. 2002.

[77] E. C. Ford, G. S. Mageras, E. Yorke, and C. C. Ling, "Respiration-correlated spiral CT: a method of measuring respiratory-induced anatomic motion for radiation treatment planning.," *Med. Phys.*, vol. 30, no. 1, pp. 88–97, Jan. 2003.

[78] E. Chin and K. Otto, "Investigation of a novel algorithm for true 4D-VMAT planning with comparison to tracked, gated and static delivery.," *Med. Phys.*, vol. 38, no. 2011, pp. 2698–2707, 2011.

[79] G. Poludniowski, M. D. R. Thomas, P. M. Evans, and S. Webb, "CT reconstruction from portal images acquired during volumetric-modulated arc therapy.," *Phys. Med. Biol.*, vol. 55, no. 19, pp. 5635–51, Oct. 2010.

[80] S. Kida, N. Saotome, Y. Masutani, H. Yamashita, K. Ohtomo, K. Nakagawa, A. Sakumi, and A. Haga, "4D-CBCT reconstruction using MV portal imaging during volumetric modulated arc therapy.," *Radiother. Oncol.*, vol. 100, no. 3, pp. 380–5, Sep. 2011.

[81] S. Yip, J. Rottmann, and R. Berbeco, "The impact of cine EPID image acquisition frame rate on markerless soft-tissue tracking," *Med. Phys.*, vol. 41, no. 6, p. 061702, Jun. 2014.

[82] H. Li, Y. Li, X. Zhang, X. Li, W. Liu, M. T. Gillin, and X. R. Zhu, "Dynamically accumulated dose and 4D accumulated dose for moving tumors.," *Med. Phys.*, vol. 39, no. 2012, pp. 7359–67, 2012.

[83] G. Starkschall, J. P. Gibbons, and C. G. Orton, "Point/counterpoint. To ensure that target volumes are not underirradiated when respiratory motion may affect the dose distribution, 4D dose calculations should be performed.," *Med. Phys.*, vol. 36, no. 2009, pp. 1–3, 2009.

[84] D. Boye, T. Lomax, and A. Knopf, "Mapping motion from 4D-MRI to 3D-CT for use in 4D dose calculations: a technical feasibility study.," *Med. Phys.*, vol. 40, p. 061702, 2013.

[85] M. K. H. Chan, D. L. W. Kwong, S. C. Y. Ng, E. K. W. Tam, and A. S. M. Tong, "Investigation of four-dimensional (4D) Monte Carlo dose calculation in real-time tumor tracking stereotatic body radiotherapy for lung cancers," *Med. Phys.*, vol. 39, no. 2012, p. 5479, 2012.

[86] S. Goossens, F. Senny, J. a Lee, G. Janssens, and X. Geets, "Assessment of tumor motion reproducibility with audio-visual coaching through successive 4D CT sessions.," *J. Appl. Clin. Med. Phys.*, vol. 15, no. 1, p. 4332, Jan. 2014.

[87] R. I. Berbeco, S. Nishioka, H. Shirato, G. T. Y. Chen, and S. B. Jiang, "Residual motion of lung tumours in gated radiotherapy with external respiratory surrogates.," *Phys. Med. Biol.*, vol. 50, no. 16, pp. 3655–67, Aug. 2005.

[88] R. George, T. D. Chung, S. S. Vedam, V. Ramakrishnan, R. Mohan, E. Weiss, and P. J. Keall, "Audio-visual biofeedback for respiratory-gated radiotherapy: impact of audio instruction and audio-visual biofeedback on respiratory-gated radiotherapy.," *Int. J. Radiat. Oncol. Biol. Phys.*, vol. 65, no. 3, pp. 924–33, Jul. 2006.

[89] J. Duan, S. Shen, J. B. Fiveash, I. a. Brezovich, R. a. Popple, and P. N. Pareek, "Dosimetric effect of respiration-gated beam on IMRT delivery," *Med. Phys.*, vol. 30, no. 8, p. 2241, 2003.

[90] G. D. Hugo, N. Agazaryan, and T. D. Solberg, "The effects of tumor motion on planning and delivery of respiratory-gated IMRT," *Med. Phys.*, vol. 30, no. 6, p. 1052, 2003.

[91] H. Onishi, K. Kuriyama, T. Komiyama, S. Tanaka, N. Sano, Y. Aikawa, Y. Tateda, T. Araki, S. Ikenaga, and M. Uematsu, "A new irradiation system for lung cancer combining linear accelerator, computed tomography, patient self-breath-holding, and patient-directed beam-control without respiratory monitoring devices.," *Int. J. Radiat. Oncol. Biol. Phys.*, vol. 56, no. 1, pp. 14–20, May 2003.

[92] M. J. Murphy, D. Martin, R. Whyte, J. Hai, C. Ozhasoglu, and Q.-T. Le, "The effectiveness of breath-holding to stabilize lung and pancreas tumors during radiosurgery.," *Int. J. Radiat. Oncol. Biol. Phys.*, vol. 53, no. 2, pp. 475–82, Jun. 2002.

[93] W. Cai, M. H. Hurwitz, C. L. Williams, S. Dhou, R. I. Berbeco, J. Seco, P. Mishra, and J. H. Lewis, "3D delivered dose assessment using a 4DCT-based motion model," *Med. Phys.*, vol. 42, no. 6, pp. 2897–2907, 2015.

[94] L. Ko, J. O. Kim, and J. V Siebers, "Investigation of the optimal backscatter for an aSi electronic portal imaging device," *Phys. Med. Biol.*, vol. 49, no. 9, pp. 1723–38, May 2004.

[95] P. Munro and D. C. Bouius, "X-ray quantum limited portal imaging using amorphous silicon flat-panel arrays," *Med. Phys.*, vol. 25, no. 5, pp. 689–702, May 1998.

[96] L. E. Antonuk, Y. El-Mohri, W. Huang, K. W. Jee, J. H. Siewerdsen, M. Maolinbay, V. E. Scarpine, H. Sandler, and J. Yorkston, "Initial performance evaluation of an indirect-detection, active matrix flat-panel imager (AMFPI) prototype for megavoltage imaging," *Int. J. Radiat. Oncol. Biol. Phys.*, vol. 42, no. 2, pp. 437–54, Sep. 1998.

[97] D. W. O. Rogers, "BEAM: A Monte Carlo code to simulate radiotherapy treatment units," *Med. Phys.*, vol. 22, no. 5, p. 503, 1995.

[98] J. W. Penelope J. Allisy-Roberts, *Farr's Physics for Medical Imaging*, 2nd ed. Saunders Ltd., 2007.

[99] F. M. Khan, *The Physics of Radiation Therapy*. Lippincott Williams & Wilkins, 2003.

[100] M. Kurudirek, "Effective atomic numbers and electron densities of some human tissues and dosimetric materials for mean energies of various radiation sources relevant to radiotherapy and medical applications," *Radiat. Phys. Chem.*, vol. 102, pp. 139–146, 2014.

[101] M. L. Taylor, R. L. Smith, F. Dossing, and R. D. Franich, "Robust calculation of effective atomic numbers: the Auto-Z(eff) software," *Med. Phys.*, vol. 39, no. 4, pp. 1769–78, Apr. 2012.

[102] V. P. Singh and N. M. Badiger, "Effective atomic numbers of some tissue substitutes by different methods: A comparative study.," *J. Med. Phys.*, vol. 39, no. 1, pp. 24–31, Jan. 2014.

[103] M. Fippel, F. Haryanto, O. Dohm, F. Nüsslin, and S. Kriesen, "A virtual photon energy fluence model for Monte Carlo dose calculation," *Med. Phys.*, vol. 30, no. 3, pp. 301–311, 2003.

[104] B. Walters, I. Kawrakow, and D. W. O. Rogers, "DOSXYZnrc Users Manual," 2011.

[105] C. L. Williams, P. Mishra, J. Seco, S. St James, R. H. Mak, R. I. Berbeco, and J. H. Lewis, "A mass-conserving 4D XCAT phantom for dose calculation and accumulation.," *Med. Phys.*, vol. 40, no. 7, p. 071728, Jul. 2013.

[106] P. Mishra, S. St. James, W. P. Segars, R. I. Berbeco, and J. H. Lewis, "Adaptation and applications of a realistic digital phantom based on patient lung tumor trajectories," *Phys. Med. Biol.*, vol. 57, no. 11, pp. 3597–3608, Jun. 2012.

[107] Y. Tian, Z. Wang, H. Ge, T. Zhang, J. Cai, C. Kelsey, D. Yoo, and F.-F. Yin, "Dosimetric comparison of treatment plans based on free breathing, maximum, and average intensity projection CTs for lung cancer SBRT," *Med. Phys.*, vol. 39, no. 5, p. 2754, 2012.

[108] M. Nakamura, Y. Narita, A. Sawada, K. Matsugi, M. Nakata, Y. Matsuo, T. Mizowaki, and M. Hiraoka, "Impact of motion velocity on four-dimensional target volumes: A phantom study," *Med. Phys.*, vol. 36, no. 5, p. 1610, 2009.

[109] J. Yoon, J. Jung, I. Yeo, J. Kim, and B. Yi, "Feasibility study of 4D image reconstruction by organ motion vector extension based on portal images (accepted)," *Med. Phys.*, 2015.